1	Zinc stimulation of phytoplankton in a low carbon dioxide, coastal Antarctic environment:
2	evidence for the Zn hypothesis
3	Riss M. Kell ^{1,+} , Adam V. Subhas ¹ , Nicole L. Schanke ² , Lauren E. Lees ³ , Rebecca J. Chmiel ¹ ,
4	Deepa Rao ¹ , Margaret M. Brisbin ¹ , Dawn M. Moran ¹ , Matthew R. McIlvin ¹ , Francesco
5	Bolinesi ⁴ , Olga Mangoni ⁴ , Raffaella Casotti ⁵ , Cecilia Balestra ⁶ , Tristan J. Horner ¹ , Robert B.
6	Dunbar ⁷ , Andrew E. Allen ^{8,9} , Giacomo R. DiTullio ² , Mak A. Saito ^{1*}
7	¹ Department of Marine Chemistry and Geochemistry, Woods Hole Oceanographic Institution,
8	Woods Hole, MA, 02543, USA
9	² Hollings Marine Laboratory, College of Charleston, Charleston, SC, 29424, USA
10	³ Department of Ecology and Evolutionary Biology, University of California at Irvine, Irvine,
11	CA, 92697, USA
12	⁴ Department of Biology, Università degli Studi di Napoli Federico II, Complesso di Monte
13	Sant'Angelo, Via Cinthia 21, 80126, Napoli, Italy
14	⁵ Department of Integrative Marine Ecology, Stazione Zoologica Anton Dohrn, Villa Comunale,
15	80121, Naples, Italy
16	⁶ National Institute of Oceanography and Applied Geophysics, 34010 Sgonico (TS), Italy
17	⁷ Doerr School of Sustainability, Stanford University, Stanford, CA, 94305, USA
18	⁸ Microbial & Environmental Genomics, J. Craig Venter Institute, San Diego, CA, 92093, USA
19	⁹ Scripps Institution of Oceanography, Integrative Oceanography Division, University of
20	California, San Diego, CA, 92037, USA
21	Correspondence to: Mak A. Saito (msaito@whoi.edu)
22	⁺ Formerly published under Riss Kellogg; now affiliated with Gloucester Marine Genomics
23	Institute, Gloucester MA, 01930

Abstract.

24

25

26

27

28

29

30

31

32

33

34

35

36

37

38

39

40

41

42

The ocean acts as a carbon sink, absorbing carbon from the atmosphere and resulting in substantial uptake of anthropogenic CO₂ emissions. As biological processes in the oceans such as net primary production (NPP) contribute significantly to this sink, understanding how they will shift in response to increasing atmospheric CO₂ is necessary to project future ocean carbon storage capacity. Macronutrient and micronutrient resource limitation within the oceans regulates NPP, and while some micronutrients such as zinc (Zn) are present at very low concentrations, their ability to limit NPP has remained unclear. Zn is a key micronutrient used by phytoplankton for a multitude of metabolic functions, yet there have been few observations of its influence on natural oceanic phytoplankton populations. In this study, we observed Zn limitation of growth in the natural phytoplankton community of Terra Nova Bay, Antarctica, in addition to primary iron (Fe) limitation. Shipboard incubation experiments amended with Zn and Fe resulted in significantly higher chlorophyll a content and dissolved inorganic carbon drawdown compared to Fe addition alone. Zn and Fe stress response proteins detected in incubation and environmental biomass provided independent verification of algal co-stress for these micronutrients. We consider total biomass and low surface ocean pCO2 as potential drivers of environmental Zn stress. This study definitively establishes that Zn limitation can occur in the modern oceans, opening up new possibility space in our understanding of nutrient regulation of NPP through geologic time, and we consider the future of oceanic Zn limitation in the face of climate change.

43 44

45

1 Introduction

Primary productivity in the oceans is a key component of the global carbon cycle and is largely controlled by the availability of nitrogen (N), phosphorus (P), and iron (Fe). Yet there is increasing evidence that other micronutrients such as zinc (Zn), cobalt (Co), and vitamin B₁₂ can also influence phytoplankton productivity, often as secondary limiting nutrients after N, P, or Fe are added (Moore et al. 2013; Browning and Moore 2023). Zn can be particularly scarce in the photic zone (Bruland 1980; Jakuba et al. 2012) where total dissolved Zn (dZn_T) can be below 0.2 nM in seawater due to biological uptake and complexation by organic ligands (Bruland 1989; Lohan et al. 2002; Baars and Croot 2011; Middag et al. 2019), which further lowers Zn bioavailability (Sunda and Huntsman 2000; Saito et al. 2008; Lhospice et al. 2017). Marine eukaryotic algae and copiotrophic bacteria possess a large metabolic demand for Zn that is on par with that of Fe (Sunda and Huntsman 2000; Mazzotta et al. 2021). Vertical profiles of dZn in the Southern Ocean have been measured previously. Zn has not historically been considered as a limiting micronutrient in the Southern Ocean due to the upwelling of nutrient-rich waters that bring dZn to nanomolar concentrations only a couple hundred meters below the surface. Yet nutrient-like profiles of dZn are evident throughout this region, with surface depletion due to biological uptake decreasing this large inventory in the upper water column (Fitzwater et al. 2000; Coale et al. 2005; Baars and Croot 2011; Sieber et al. 2020; Kell et al. 2024). (Coale et al. 2005; Baars and Croot 2011). Additionally, both modelbased estimates (Roshan et al. 2018) and direct field measurements (Kell et al. 2024) of Zn uptake in this region have demonstrated a substantial biological demand for Zn in surface waters, leading to significant dZn drawdown. This is consistent with and genomic and laboratory studies indicating an elevated Zn demand in polar phytoplankton (Twining and Baines 2013; Ye et al. 2022).

46

47

48

49

50

51

52

53

54

55

56

57

58

59

60

61

62

63

64

65

66

67

-Despite the scarcity of bioavailable Zn in the surface ocean and its high cellular demand, relatively few experimental studies have examined the ability of Zn addition to stimulate natural phytoplankton communities (Supplementary Table 1). These results have been variable with findings that include negative results (Scharek et al. 1997; Coale et al. 2003; Ellwood 2004), slight Zn stimulatory results (Crawford et al. 2003b), a "very small increase" relative to controls in an unreplicated experiment (Coale et al. 2003), Zn stimulation within Fe and Si uptake experiments (Franck et al. 2003), Zn primary and secondary limitation in the North Pacific in an unreplicated experiment (Jakuba et al. 2012), secondary Zn limitation after primary Si limitation in the Costa Rica Dome (Dreux Chappell et al. 2016), and enhanced Zn uptake rates under low pCO₂ (Xu et al. 2012). Whether due to the early negative results, the few positive findings, or the practical constraints of co-limitation studies in the field that limit the number of micronutrients that can be tested general prejudice against considering additional factors in controlling marine productivity, it is our experience that there is currently no broad community recognition that zinc limitation is a process that could affect primary productivity in any region of the oceans, leaving the original 'zinc hypothesis' unresolved (Morel et al. 1994).

In contrastjuxtaposition, laboratory studies have unequivocally demonstrated that marine phytoplankton can easily be Zn-limited in culture, and that Zn stress is exacerbated by low CO₂ due to an inability to synthesize the metalloenzyme carbonic anhydrase and resultant carbon colimitation (Morel et al. 1994; Buitenhuis et al. 2003; Sunda and Huntsman 2005). In this study, we reconcile these perspectives with a comprehensive, multipronged study of the natural phytoplankton assemblage in Terra Nova Bay (TNB), Antarctica, documenting evidence of Fe and Zn stress in a low pCO₂ coastal environment.

2 Results

2.1 Biogeochemical characterization of Terra Nova Bay

92

93

94

95

96

97

98

99

100

101

102

103

104

105

106

107

108

109

110

111

112

113

114

Twenty-six stations within Terra Nova Bay (TNB) were, Antarctica, was temporally sampled temporally sampled-over the course offor over one month (January 9 – February 18, 2018) during the 2017-2018 CICLOPS expedition (Fig. 1a; Supplementary Table 2) to concurrently characterize the natural progression of the phytoplankton bloom and biogeochemical changes in the water column (Kell et al. 2024). These stations were spatially distinct (each unique station was sampled once), but given that all stations were in relatively close proximity to each other within TNB (within a 52 km radius), we have combined all TNB station data to create a temporal analysis of the region. Surface waters within TNB had low (~200 μatm) seawater pCO₂ (Fig. 1b) which contrasted with measurements >400 µatm further from the study site (Fig. 1c). A large phytoplankton bloom was present as indicated by high (> 3000 ng L⁻¹) chlorophyll fluorescence concentrations in January that waned into February (Fig. 1d). This observation of high productivity is, characteristic of Antarctic polynya environments, which are recurring regions of open water surrounded by sea ice (Arrigo et al. 2012)... This phytoplankton community initially consisted of a mixed assemblage of both diatoms as indicated by fucoxanthin (fuco, Fig. 1e) and the haptophyte Phaeocystis as verified by shipboard microscopy and as indicated by 19'hexanoyloxyfucoxanthin (19'-hex, Fig. 1f). Surface fucoxanthin concentrations >200 ng L⁻¹ were observed at the late TNB stations (Fig. 1e) while 19'-hex decreased to ~20 ng L⁻¹ (Fig. 1f), indicating that the stations sampled in late February were dominated by diatoms rather than Phaeocystis. This was consistent with historical observations of phytoplankton succession patterns in TNB (DiTullio and Smith 1996; Smith et al. 2006; Mangoni et al. 2019).

Additionally, we observed pronounced depletion of total dissolved Zn in surface waters across

all TNB stations, with an average concentration of 0.82 ± 0.47 nM at 10 m (Fig. 1g). Notably, as the bloom progressed, this depletion extended progressively deeper into the water column (Fig. 1g), indicative of strong Zn uptake and export from the euphotic zone.

Pronounced and progressively deepening total dissolved Zn (dZn_T) depletion over time was observed, with dZn depleted down to an average of 0.82 ± 0.47 nM at 10 m over all TNB stations (**Fig. 1g**).

The Zn-depleted area of the water column progressively deepened to 50 m and then to -100 m throughout January and February (Fig. 1g), indicative of strong Zn uptake and export from the euphotic zone. Total Zn uptake (ρ Zn, measured concurrently using a stable isotope tracer method) (Kell et al. 2024) was highest in the shallow euphotic zone in early January and waned into February (Fig. 1h), following trends seen in chlorophyll fluorescence (Fig. 1d) and 19'-hex (Fig. 1f). This ρ Zn trend was consistent with laboratory studies demonstrating the substantial Zn requirements of both diatoms and *Phaeocystis antarctica* (Saito and Goepfert 2008; Kellogg et al. 2020). Across all TNB stations, total dissolved Fe (dFe_T) in the upper 50 m remained below 1 nM (Fig. 1i) as observed previously in this region (Fitzwater et al. 2000). In the Ross Sea, dissolved iron (dFe) has previously been demonstrated to be the primary limiting nutrient for phytoplankton growth (Martin et al. 1990; Coale et al. 2003; Sedwick et al. 2011).

2.2 Biogeochemical characterization of the incubation study site

Within TNB station, station 27 (referred to as the "experimental site" herein) was chosen for the multifactor shipboard incubation experiment (**Fig. 1a,b**; red star). This site harbored a coastal bloom and was biologically and chemically characterized as having high *in situ* chlorophyll *a* levels (maximum of 3259 ng L⁻¹ at 30 m; **Fig. 1j**) and was comprised of diatoms as

indicated by fucoxanthin and *Phaeocystis* as indicated by 19'-hex (**Fig. 1k**). A decrease in surface total dissolved inorganic carbon (DIC_T; 2181 μ mol kg⁻¹ at 15 m compared to the deep water (200-1065 m) average of 2224 \pm 2.1 μ mol kg⁻¹, **Fig. 1l**) was also observed. Within the water column, dZn demonstrated a pronounced decrease from 5.1 nM at 50 m to 0.9 nM at 10 m, representing an 82% decrease (and a 76% decrease comparing the minimum dZn_T value at 10 m to the average deepwater (210 – 1000 m) concentration of 3.9 nM \pm 0.4; **Fig. 1m**), consistent with prior observations of surface dZn depletion in this region (Fitzwater et al. 2000).

Observations of rapid Zn uptake (46 pmol L⁻¹ d⁻¹ at 10 m) at the experimental site (**Fig. 1n**) likely contributed to this surface depletion, as Zn uptake rates of this magnitude are of the appropriate scale to induce the multi-nanomolar surface water depletion during the austral spring and summer season (Kell et al. 2024). Consistent with high macronutrient abundance in this region, surface macronutrient concentrations (nitrate and nitrite, phosphate, and silicie acid) were partially depleted at the experimental site with 64%, 46%, and 29% decreases in-<u>nitrate+nitrite</u> (N+N), phosphate (P), and silicate (Si)N+N, P, and Si, respectively, comparing 10 m and average deep water (200 – 1000 m) values (**Fig. 1o**).

2.3 Evidence for Zn stimulation of phytoplankton: experimental site shipboard incubations

A multifactor incubation experiment was conducted using surface waters collected at the experimental site by trace metal clean fish sampler (7 m) fed into a shipboard cleanroom to examine controls on net primary productivity, with triplicate treatments of Zn amended (+Zn; 2 nM as ZnCl₂), Fe amended (+Fe; 1 nM as FeCl₂), and Fe and Zn amended (+Fe+Zn) incubations, in addition to unamended controls. Addition of Fe alone (+Fe) resulted in significantly higher chl a content compared to controls (p = 9.5e-5) after six days (T6) (Fig. 2a), demonstrating primary

Fe limitation as observed previously in the Ross Sea (Martin et al. 1990; Mangoni et al. 2019). However, addition of Zn alone (+Zn) also resulted in significantly higher chl a content compared to the controls (p = 0.011), implying that a subset of the incubated phytoplankton population benefitted from the addition of Zn alone, without additional Fe (Fig. 2a). This observation is consistent with independent co-limitation, and may thus have been (Saito et al. 2008), where two nutrients (such as Fe and Zn) each independently limit different subpopulations or processes, and adding either nutrient alone yields a response experiencing primary Zn limitation (Fig. 2a). The combined addition of +Fe+Zn resulted in the highest average chl a content among all treatments at T6, with $4.5 \pm 0.21 \ \mu g \ L^{-1}$ compared to $3.9 \pm 0.35 \ \mu g \ L^{-1}$ and $2.8 \pm 0.15 \ \mu g \ L^{-1}$ achieved by +Fe and +Zn alone, respectively, demonstrating additive co-limitation between Zn and Fe (Sperfeld et al. 2016). The Zn stock solution was analyzed to confirm these results were not caused by inadvertent Feiron contamination (see Methods). Significant differences in seawater chemistry were also observed within these incubations over time, with larger decreases in DIC_T in all metal treatments compared to the control (-12.7 μ mol kg⁻¹ for +Fe (p = 5.3e-6), -8.2 μ mol kg⁻¹ for +Zn (p = 5e-5), and -18.5 μ mol kg⁻¹ for +Fe+Zn (p = 2.2e-16); **Fig. 2b**). The decrease in DIC_T observed with +Fe+Zn was significantly larger than that achieved with +Fe alone (p = 4.4e-3; Fig. 2b). Statistically significant differences in measured parameters among treatments are summarized in Supplementary Table 3.

161

162

163

164

165

166

167

168

169

170

171

172

173

174

175

176

177

178

179

180

181

182

183

Further consistent with the observed Zn stimulation of biomass in the incubations, the largest decreases in macronutrient (P and N+N) concentrations in these incubations at T6 were observed in the +Fe+Zn treatment (**Supplementary Figure 1a,b**), as was the largest increase in particulate organic carbon (POC; **Supplementary Figure 1c**). POC collected from the +Zn and +Fe+Zn incubations was characterized by larger C:N atomic ratios (5.9 and 6.2, respectively)

Formatted: Font: Bold

Formatted: Font: Not Bold

compared to the +Fe and T6 control (5.2 and 5.3; **Supplementary Figure 1d**). Significantly higher bacterial abundances in both +Fe (p = 9.1e-4) and +Fe+Zn (p = 6.3e-4) treatments relative to the T6 control (**Supplementary Figure 1e**) indicated the alleviation of bacterial Fe limitation, consistent with prior reports (Obernosterer et al. 2015; Fourquez et al. 2020; Sun et al. 2021).

184

185

186

187

188

189

190

191

192

193

194

195

196

197

198

199

200

201

202

203

204

205

206

At the conclusion of the incubation experiments, biomass was collected by serial filtration through 5 mm and 0.2 mm filters, and the 0.2-5 umm fraction was extracted for proteomic analysis was performed (see Methods) and analyzed for biomarkers of Zn and Fe stress. We detected both algal Fe- and Zn-stress proteins, which provided an independent line of evidence corroborating the results described above (Fig. 2c). This included the detection of the Zn/Co responsive protein ZCRP-A (a putative Zn chaperone) (Kellogg et al. 2022a) as a biomarker of Zn stress as well as the iron starvation-induced proteins ISIP1A, ISIP2A and ISIP3 (ISIPs) as biomarkers of Fe stress (Supplementary Table 4). The ISIPs represent a group of unrelated proteins that are upregulated under Fe limitation in various algal species. ISIP1 proteins are responsible for endocytosis of siderophore-bound iron, ISIP2 proteins are involved in Fe³⁺ uptake, and ISIP3 has been suggested to act as an Fe storage protein (Allen et al. 2008; Behnke and LaRoche 2020). RUBISCO abundance within each treatment is shown in Fig. 2c as a proxy for the potential phytoplankton production. Within the T6 incubation biomass, there was an increased abundance of ISIPs in the control and +Zn treatment, and a decrease in ISIP protein abundance within the +Fe and +Fe+Zn treatments, consistent with primary Fe limitation and the expected response to Fe addition (Fig. 2c). ISIPs were taxonomically assigned to diatoms, Phaeocystis, and dinoflagellates (Fig. 2d). The strongest expression of ZCRP-A protein was detected in the +Fe treatment (Fig. 2c,d) indicative of Fe addition driving the community towards increased Zn stress. Notably, ZCRP-A was still detected in the +Fe+Zn treatment (Fig.

2c,d), implying that the added Zn was unable to completely satiate Zn demand as phytoplankton biomass increased (as indicated by the increase in chl *a* at T6, Fig. 2a), despite added Zn (2 nM) being double that of added Fe (1 nM). Sequence analysis of the contigs identified as ZCRP-A homologs in these incubations revealed that all contigs contained one or more canonical conserved motifs found in COG0523 family proteins such as ZCRP-A (Supplementary Figure 2). Coupled with evidence from prior laboratory studies (Kellogg et al. 2022a), this provides further support for the role of ZCRP-A in responding to Zn scarcity. ZCRP-A proteins were taxonomically assigned to chlorophytes, dinoflagellates, and *Phaeocystis*, with the detection of *Phaeocystis* ZCRP-A only in the +Fe treatment (Fig. 2d). The detection of ZCRP-A attributed to *Phaeocystis*, but the nondetection of ZCRP-A attributed to diatoms₃ implies that either ample diatom biomass was not captured on the analyzed filters due to being filtered out by the >5 mum pre-filter, or that diatoms present in these incubations (as indicated by diatom RUBISCO; Fig. 2d) were outcompeting *Phaeocystis* for Zn. Our observations of Fe and Zn biomarkers shifting in abundance in response to their respective metal treatment provides independent evidence for Zn/Fe co-limitation.

223 2.4 Taxonomic characterization of incubation results

To characterize the phytoplankton species responding to metal amendment, we measured phytoplankton pigments within the shipboard incubations over time, which revealed a diverse taxonomic response to metal amendments. Measured pigments included fucoxanthin (fuco), 19'-hexanoyloxyfucoxanthin (19'-hex), prasinoxanthin (prasino), chlorophyll *b* (chl *b*), and chlorophyll c3 (chl c3). Fuco is produced by both diatoms and by *Phaeocystis* under certain conditions, while 19'-hex and chl c3 are indicative of *Phaeocystis* in the Southern Ocean

(DiTullio et al. 2007). Fuco: 19'-hex ratios significantly increased in the +Fe (p = 4.2e-4) and +Fe+Zn treatments (p = 2.7e-3) (Supplementary Figure 3a) due to no significant change in fuco (Supplementary Figure 3b) and decreased 19'-hex (Supplementary Figure 3c) relative to the T6 control. Phaeocystis contributions to total fuco concentrations are typically minimal at the low Fe levels of the Ross Sea, though *Phaeocystis* can revert to making fuco rather than 19'-hex when released from Fe limitation (DiTullio et al. 2007), as was evident in these incubations by decreased 19'-hex:chl c3 ratios within the +Fe and +Fe+Zn treatments (Supplementary Figure **3d**). *Phaeocystis* therefore likely contributed to total fuco by responding to Fe addition. Notably, significant decreases in both fuco:chl a and 19'-hex:chl a (Supplementary Figure 3e,f) in all treatments compared to the T6 control indicated that other phytoplankton groups contributed to chl a (Fig. 2a) without contributing fuco nor 19'hex. Increases in chl b (Supplementary Figure 3g) and prasinoxanthin (Supplementary Figure 3h) suggest that small green algae such as chlorophytes and prasinophytes also responded to +Fe and +Zn independently, consistent with the detection of chlorophyte ZCRP-A in these incubations (Fig. 2d). Photosynthetic efficiency of photosystem II (Fv/Fm) significantly increased with +Fe (p = 0.011) and with +Fe+Zn (p =0.0036) at T4 (day 4) compared to T4 controls, but did not significantly increase with +Zn alone, implying Fv/Fm may not be useful as a diagnostic for Zn stress and that caution should be used in interpreting its signals universally (Supplementary Figure 3i). No significant difference in Fv/Fm was observed among treatments at T6. Selective zooplankton grazing on small diatoms and solitary Phaeocystis cells may have played a role in affecting phytoplankton biomass and the observed pigment:chl a ratios. For instance, higher ratios of phaeophytin:total phaeopigments were observed in +Fe and +Zn amended incubations (Supplementary Figure 4) which may reflect grazing on solitary *Phaeocystis* cells, as high phaeophytin:total phaeopigments ratios were

230

231

232

233

234

235

236

237

238

239

240

241

242

243

244

245

246

247

248

249

250

251

previously observed in *Phaeocystis* dominated waters of the Ross Sea (DiTullio and Smith 1996).

2.5 Detection of Zn- and Fe-stress protein biomarkers in the water column

Metaproteomic and metatranscriptomic analyses of biomass within the water column at the experimental site provided additional confirmation of the incubation results, as we detected Zn- and Fe- stress-response proteins present within the water column, which were therefore naturally present without influence from incubation conditions. In addition to ISIPs and ZCRP-A, we detected ZCRP-B (a putative membrane-tethered Zn-binding protein) (Kellogg et al. 2022a), Zrt/Irt-like (ZIP) Zn transporters (which are known to be used by marine phytoplankton for uptake of Zn²⁺ and other divalent metal cations (Allen et al. 2008; Milner et al. 2013; Bender et al. 2018)), and θ (theta) and δ (delta) carbonic anhydrases (CAs). θ -CAs with Zn²⁺ coordination sites have been documented in diatoms (Jensen et al. 2020a), including the polar diatom *Chaetoceros neogracile* RS19 (Kellogg et al. 2022b), but no studies to date have investigated enzyme activity nor efficiency with Co²⁺ or Cd²⁺. In contrast, δ -CA (i.e, *Thalassiosira weissflogii* TWCA1) is known to function with either Co²⁺ or Zn²⁺ as a cofactor (Lane and Morel 2000b) conferring metabolic flexibility when Zn²⁺ is scarce.

Both proteins and transcripts of Zn and Fe stress biomarkers (ZCRP-A and ISIPs) were observed throughout the water column at the experimental site. RUBISCO, ZCRP-A, and ISIP protein spectral counts were most abundant at the surface and decreased with depth within the within the 3μm size fraction (**Fig. 3a-c**), consistent with the depletion of trace metals in the photic zone due to high-biomass bloom conditions. ZCRP-A was detected in both 3 and 51 μm filter pore-size fractions (**Fig. 3b**) and was predominantly attributed to *Phaeocystis* and the diatom genus *Chaetoceros* in the euphotic zone, and predominantly to *Phaeocystis* and the

The presence of <i>Phaeocystis</i> below the photic zone is consistent with prior observations of rapid export of <i>Phaeocystis</i> cells (DiTullio et al. 2000). Throughout the water column, ISIPs were predominantly attributed to <i>Phaeocystis</i> and to the diatom genera <i>Fragilariopsis</i> , <i>Chaetoceros</i> , and <i>Pseudo-nitzschia</i> (Fig. 3i, Supplementary Figure 5b). We note that ZCRP-B, a protein also found to be upregulated in marine diatoms under low Zn/Co and characterized as a putative membrane-tethered Zn/Co protein ligand (Kellogg et al. 2022a) was most abundant in the 0.2 µm fraction throughout the water column (Fig. 3d). As ZCRP-B shares ~30% similarity to the bacterial ABC-type nickel transporter component NikA, spectral counts within the bacterial 0.2 µm fraction most likely reflect true bacterial NikA. BLAST analysis of all ZCRP-B contigs confirmed that all ZCRP-B hits across all size fractions corresponded to bacteria (Fig. 3i). ZIPs were almost solely detected in the 51 µm fraction, likely due to the capture of abundant <i>Phaeocystis</i> colonies and chain-forming diatoms (Fig. 3e; Supplementary Figure 5e). The assignment of the majority of ZCRP-A and ISIP proteins to <i>Phaeocystis</i> in the upper water column provides additional evidence that <i>Phaeocystis</i> was likely Zn/Fe co-limited at the study site, consistent with incubation results (Fig. 2d). ZCRP-A belongs to the phylogenetically complex COG0523 family, with some family members showing functional divergence (that is, activity using different metal cofactors) among paralogs (Blaby-Haas and Merchant 2012; Edmonds et al. 2021). Here, we infer a Zn-responsive function for the identified ZCRP-A contigs based on their homology to <i>T. pseudonana</i> and <i>P. tricornutum</i> ZCRP-A proteins, which we have previously characterized as Zn-responsive (Kellogg et al. 2022a). To further support this inference, we used SHOOT (Emms and Kelly	diatom genus <i>Pseudo-nitzschia</i> in the mesopelagic zone (Fig. 3i, Supplementary Figure 5a).
predominantly attributed to <i>Phaeocystis</i> and to the diatom genera <i>Fragilariopsis</i> , <i>Chaetoceros</i> , and <i>Pseudo-nitzschia</i> (Fig. 3i , Supplementary Figure 5b). We note that ZCRP-B, a protein also found to be upregulated in marine diatoms under low Zn/Co and characterized as a putative membrane-tethered Zn/Co protein ligand (Kellogg et al. 2022a) was most abundant in the 0.2 µm fraction throughout the water column (Fig. 3d). As ZCRP-B shares ~30% similarity to the bacterial ABC-type nickel transporter component NikA, spectral counts within the bacterial 0.2 µm fraction most likely reflect true bacterial NikA. BLAST analysis of all ZCRP-B contigs confirmed that all ZCRP-B hits across all size fractions corresponded to bacteria (Fig. 3i). ZIPs were almost solely detected in the 51 µm fraction, likely due to the capture of abundant <i>Phaeocystis</i> colonies and chain forming diatoms (Fig. 3e; Supplementary Figure 5e). The assignment of the majority of ZCRP-A and ISIP proteins to <i>Phaeocystis</i> in the upper water column provides additional evidence that <i>Phaeocystis</i> was likely Zn/Fe co-limited at the study site, consistent with incubation results (Fig. 2d). ZCRP-A belongs to the phylogenetically complex COG0523 family, with some family members showing functional divergence (that is, activity using different metal cofactors) among paralogs (Blaby-Haas and Merchant 2012; Edmonds et al. 2021). Here, we infer a Zn-responsive function for the identified ZCRP-A contigs based on their homology to <i>T. pseudonana</i> and <i>P. tricormutum</i> ZCRP-A proteins, which we have previously characterized as Zn-responsive	The presence of <i>Phaeocystis</i> below the photic zone is consistent with prior observations of rapid
and Pseudo-nitzschia (Fig. 3i, Supplementary Figure 5b). We note that ZCRP-B, a protein also found to be upregulated in marine diatoms under low Zn/Co and characterized as a putative membrane-tethered Zn/Co protein ligand (Kellogg et al. 2022a) was most abundant in the 0.2 µm fraction throughout the water column (Fig. 3d). As ZCRP-B shares ~30% similarity to the bacterial ABC-type nickel transporter component NikA, spectral counts within the bacterial 0.2 µm fraction most likely reflect true bacterial NikA. BLAST analysis of all ZCRP-B contigs confirmed that all ZCRP-B hits across all size fractions corresponded to bacteria (Fig. 3i). ZIPs were almost solely detected in the 51 µm fraction, likely due to the capture of abundant Phaeocystis colonies and chain forming diatoms (Fig. 3e; Supplementary Figure 5e). The assignment of the majority of ZCRP-A and ISIP proteins to Phaeocystis in the upper water column provides additional evidence that Phaeocystis was likely Zn/Fe co-limited at the study site, consistent with incubation results (Fig. 2d). ZCRP-A belongs to the phylogenetically complex COG0523 family, with some family members showing functional divergence (that is, activity using different metal cofactors) among paralogs (Blaby-Haas and Merchant 2012; Edmonds et al. 2021). Here, we infer a Zn-responsive function for the identified ZCRP-A contigs based on their homology to T. pseudonana and P. tricornutum ZCRP-A proteins, which we have previously characterized as Zn-responsive	export of <i>Phaeocystis</i> cells (DiTullio et al. 2000). Throughout the water column, ISIPs were
found to be upregulated in marine diatoms under low Zn/Co and characterized as a putative membrane-tethered Zn/Co protein ligand (Kellogg et al. 2022a) was most abundant in the 0.2 μm fraction throughout the water column (Fig. 3d). As ZCRP-B shares ~30% similarity to the bacterial ABC-type nickel transporter component NikA, spectral counts within the bacterial 0.2 μm fraction most likely reflect true bacterial NikA. BLAST analysis of all ZCRP-B contigs confirmed that all ZCRP-B hits across all size fractions corresponded to bacteria (Fig. 3i). ZIPs were almost solely detected in the 51 μm fraction, likely due to the capture of abundant <i>Phaeocystis</i> colonies and chain-forming diatoms (Fig. 3e; Supplementary Figure 5e). The assignment of the majority of ZCRP-A and ISIP proteins to <i>Phaeocystis</i> in the upper water column provides additional evidence that <i>Phaeocystis</i> was likely Zn/Fe co-limited at the study site, consistent with incubation results (Fig. 2d). ZCRP-A belongs to the phylogenetically complex COG0523 family, with some family members showing functional divergence (that is, activity using different metal cofactors) among paralogs (Blaby-Haas and Merchant 2012; Edmonds et al. 2021). Here, we infer a Zn-responsive function for the identified ZCRP-A contigs based on their homology to <i>T. pseudonana</i> and <i>P. tricornutum</i> ZCRP-A proteins, which we have previously characterized as Zn-responsive	predominantly attributed to <i>Phaeocystis</i> and to the diatom genera <i>Fragilariopsis</i> , <i>Chaetoceros</i> ,
membrane-tethered Zn/Co protein ligand (Kellogg et al. 2022a) was most abundant in the 0.2 µm fraction throughout the water column (Fig. 3d). As ZCRP-B shares ~30% similarity to the bacterial ABC-type nickel transporter component NikA, spectral counts within the bacterial 0.2 µm fraction most likely reflect true bacterial NikA. BLAST analysis of all ZCRP-B contigs confirmed that all ZCRP-B hits across all size fractions corresponded to bacteria (Fig. 3i). ZIPs were almost solely detected in the 51 µm fraction, likely due to the capture of abundant <i>Phaeocystis</i> colonies and chain-forming diatoms (Fig. 3e; Supplementary Figure 5e). The assignment of the majority of ZCRP-A and ISIP proteins to <i>Phaeocystis</i> in the upper water column provides additional evidence that <i>Phaeocystis</i> was likely Zn/Fe co-limited at the study site, consistent with incubation results (Fig. 2d). ZCRP-A belongs to the phylogenetically complex COG0523 family, with some family members showing functional divergence (that is, activity using different metal cofactors) among paralogs (Blaby-Haas and Merchant 2012; Edmonds et al. 2021). Here, we infer a Zn-responsive function for the identified ZCRP-A contigs based on their homology to <i>T. pseudonana</i> and <i>P. tricornutum</i> ZCRP-A proteins, which we have previously characterized as Zn-responsive	and Pseudo-nitzschia (Fig. 3i, Supplementary Figure 5b). We note that ZCRP-B, a protein also
fraction throughout the water column (Fig. 3d). As ZCRP-B shares ~30% similarity to the bacterial ABC-type nickel transporter component NikA, spectral counts within the bacterial 0.2 µm fraction most likely reflect true bacterial NikA. BLAST analysis of all ZCRP-B contigs confirmed that all ZCRP-B hits across all size fractions corresponded to bacteria (Fig. 3i). ZIPs were almost solely detected in the 51 µm fraction, likely due to the capture of abundant <i>Phaeocystis</i> colonies and chain-forming diatoms (Fig. 3e; Supplementary Figure 5e). The assignment of the majority of ZCRP-A and ISIP proteins to <i>Phaeocystis</i> in the upper water column provides additional evidence that <i>Phaeocystis</i> was likely Zn/Fe co-limited at the study site, consistent with incubation results (Fig. 2d). ZCRP-A belongs to the phylogenetically complex COG0523 family, with some family members showing functional divergence (that is, activity using different metal cofactors) among paralogs (Blaby-Haas and Merchant 2012; Edmonds et al. 2021). Here, we infer a Zn-responsive function for the identified ZCRP-A contigs based on their homology to <i>T. pseudonana</i> and <i>P. tricornutum</i> ZCRP-A proteins, which we have previously characterized as Zn-responsive	found to be upregulated in marine diatoms under low Zn/Co and characterized as a putative
bacterial ABC-type nickel transporter component NikA, spectral counts within the bacterial 0.2 µm fraction most likely reflect true bacterial NikA. BLAST analysis of all ZCRP-B contigs confirmed that all ZCRP-B hits across all size fractions corresponded to bacteria (Fig. 3i). ZIPs were almost solely detected in the 51 µm fraction, likely due to the capture of abundant Phaeocystis colonies and chain-forming diatoms (Fig. 3e; Supplementary Figure 5c). The assignment of the majority of ZCRP-A and ISIP proteins to Phaeocystis in the upper water column provides additional evidence that Phaeocystis was likely Zn/Fe co-limited at the study site, consistent with incubation results (Fig. 2d). ZCRP-A belongs to the phylogenetically complex COG0523 family, with some family members showing functional divergence (that is, activity using different metal cofactors) among paralogs (Blaby-Haas and Merchant 2012; Edmonds et al. 2021). Here, we infer a Zn-responsive function for the identified ZCRP-A contigs based on their homology to T. pseudonana and P. tricornutum ZCRP-A proteins, which we have previously characterized as Zn-responsive	membrane-tethered Zn/Co protein ligand (Kellogg et al. 2022a) was most abundant in the 0.2 μm
μm fraction most likely reflect true bacterial NikA. BLAST analysis of all ZCRP-B contigs confirmed that all ZCRP-B hits across all size fractions corresponded to bacteria (Fig. 3i). ZIPs were almost solely detected in the 51 μm fraction, likely due to the capture of abundant <i>Phaeocystis</i> colonies and chain-forming diatoms (Fig. 3e ; Supplementary Figure 5e). The assignment of the majority of ZCRP-A and ISIP proteins to <i>Phaeocystis</i> in the upper water column provides additional evidence that <i>Phaeocystis</i> was likely Zn/Fe co-limited at the study site, consistent with incubation results (Fig. 2d). ZCRP-A belongs to the phylogenetically complex COG0523 family, with some family members showing functional divergence (that is, activity using different metal cofactors) among paralogs (Blaby-Haas and Merchant 2012; Edmonds et al. 2021). Here, we infer a Zn-responsive function for the identified ZCRP-A contigs based on their homology to <i>T. pseudonana</i> and <i>P. tricornutum</i> ZCRP-A proteins, which we have previously characterized as Zn-responsive	fraction throughout the water column (Fig. 3d). As ZCRP-B shares ${\sim}30\%$ similarity to the
confirmed that all ZCRP-B hits across all size fractions corresponded to bacteria (Fig. 3i). ZIPs were almost solely detected in the 51 µm fraction, likely due to the capture of abundant <i>Phaeocystis</i> colonies and chain-forming diatoms (Fig. 3e; Supplementary Figure 5e). The assignment of the majority of ZCRP-A and ISIP proteins to <i>Phaeocystis</i> in the upper water column provides additional evidence that <i>Phaeocystis</i> was likely Zn/Fe co-limited at the study site, consistent with incubation results (Fig. 2d). ZCRP-A belongs to the phylogenetically complex COG0523 family, with some family members showing functional divergence (that is, activity using different metal cofactors) among paralogs (Blaby-Haas and Merchant 2012; Edmonds et al. 2021). Here, we infer a Zn-responsive function for the identified ZCRP-A contigs based on their homology to <i>T. pseudonana</i> and <i>P. tricornutum</i> ZCRP-A proteins, which we have previously characterized as Zn-responsive	bacterial ABC-type nickel transporter component NikA, spectral counts within the bacterial 0.2
ZIPs were almost solely detected in the 51 µm fraction, likely due to the capture of abundant <i>Phaeocystis</i> colonies and chain forming diatoms (Fig. 3e; Supplementary Figure 5c). The assignment of the majority of ZCRP-A and ISIP proteins to <i>Phaeocystis</i> in the upper water column provides additional evidence that <i>Phaeocystis</i> was likely Zn/Fe co-limited at the study site, consistent with incubation results (Fig. 2d). ZCRP-A belongs to the phylogenetically complex COG0523 family, with some family members showing functional divergence (that is, activity using different metal cofactors) among paralogs (Blaby-Haas and Merchant 2012; Edmonds et al. 2021). Here, we infer a Zn-responsive function for the identified ZCRP-A contigs based on their homology to <i>T. pseudonana</i> and <i>P. tricornutum</i> ZCRP-A proteins, which we have previously characterized as Zn-responsive	μm fraction most likely reflect true bacterial NikA. BLAST analysis of all ZCRP-B contigs
abundant <i>Phaeocystis</i> colonies and chain-forming diatoms (Fig. 3e ; Supplementary Figure 5c). The assignment of the majority of ZCRP-A and ISIP proteins to <i>Phaeocystis</i> in the upper water column provides additional evidence that <i>Phaeocystis</i> was likely Zn/Fe co-limited at the study site, consistent with incubation results (Fig. 2d). ZCRP-A belongs to the phylogenetically complex COG0523 family, with some family members showing functional divergence (that is, activity using different metal cofactors) among paralogs (Blaby-Haas and Merchant 2012; Edmonds et al. 2021). Here, we infer a Zn-responsive function for the identified ZCRP-A contigs based on their homology to <i>T. pseudonana</i> and <i>P. tricornutum</i> ZCRP-A proteins, which we have previously characterized as Zn-responsive	confirmed that all ZCRP-B hits across all size fractions corresponded to bacteria (Fig. 3i).
The assignment of the majority of ZCRP-A and ISIP proteins to <i>Phaeocystis</i> in the upper water column provides additional evidence that <i>Phaeocystis</i> was likely Zn/Fe co-limited at the study site, consistent with incubation results (Fig. 2d). ZCRP-A belongs to the phylogenetically complex COG0523 family, with some family members showing functional divergence (that is, activity using different metal cofactors) among paralogs (Blaby-Haas and Merchant 2012; Edmonds et al. 2021). Here, we infer a Zn-responsive function for the identified ZCRP-A contigs based on their homology to <i>T. pseudonana</i> and <i>P. tricornutum</i> ZCRP-A proteins, which we have previously characterized as Zn-responsive	ZIPs were almost solely detected in the 51 µm fraction, likely due to the capture of
column provides additional evidence that <i>Phaeocystis</i> was likely Zn/Fe co-limited at the study site, consistent with incubation results (Fig. 2d). ZCRP-A belongs to the phylogenetically complex COG0523 family, with some family members showing functional divergence (that is, activity using different metal cofactors) among paralogs (Blaby-Haas and Merchant 2012; Edmonds et al. 2021). Here, we infer a Zn-responsive function for the identified ZCRP-A contigs based on their homology to <i>T. pseudonana</i> and <i>P. tricornutum</i> ZCRP-A proteins, which we have previously characterized as Zn-responsive	abundant Phaeocystis colonies and chain-forming diatoms (Fig. 3e; Supplementary Figure 5c).
site, consistent with incubation results (Fig. 2d). ZCRP-A belongs to the phylogenetically complex COG0523 family, with some family members showing functional divergence (that is, activity using different metal cofactors) among paralogs (Blaby-Haas and Merchant 2012; Edmonds et al. 2021). Here, we infer a Zn-responsive function for the identified ZCRP-A contigs based on their homology to <i>T. pseudonana</i> and <i>P. tricornutum</i> ZCRP-A proteins, which we have previously characterized as Zn-responsive	The assignment of the majority of ZCRP-A and ISIP proteins to <i>Phaeocystis</i> in the upper water
ZCRP-A belongs to the phylogenetically complex COG0523 family, with some family members showing functional divergence (that is, activity using different metal cofactors) among paralogs (Blaby-Haas and Merchant 2012; Edmonds et al. 2021). Here, we infer a Zn-responsive function for the identified ZCRP-A contigs based on their homology to <i>T. pseudonana</i> and <i>P. tricornutum</i> ZCRP-A proteins, which we have previously characterized as Zn-responsive	column provides additional evidence that <i>Phaeocystis</i> was likely Zn/Fe co-limited at the study
members showing functional divergence (that is, activity using different metal cofactors) among paralogs (Blaby-Haas and Merchant 2012; Edmonds et al. 2021). Here, we infer a Zn-responsive function for the identified ZCRP-A contigs based on their homology to <i>T. pseudonana</i> and <i>P. tricornutum</i> ZCRP-A proteins, which we have previously characterized as Zn-responsive	site, consistent with incubation results (Fig. 2d).
paralogs (Blaby-Haas and Merchant 2012; Edmonds et al. 2021). Here, we infer a Zn-responsive function for the identified ZCRP-A contigs based on their homology to <i>T. pseudonana</i> and <i>P. tricornutum</i> ZCRP-A proteins, which we have previously characterized as Zn-responsive	ZCRP-A belongs to the phylogenetically complex COG0523 family, with some family
function for the identified ZCRP-A contigs based on their homology to <i>T. pseudonana</i> and <i>P. tricornutum</i> ZCRP-A proteins, which we have previously characterized as Zn-responsive	members showing functional divergence (that is, activity using different metal cofactors) among
tricornutum ZCRP-A proteins, which we have previously characterized as Zn-responsive	paralogs (Blaby-Haas and Merchant 2012; Edmonds et al. 2021). Here, we infer a Zn-responsive
	function for the identified ZCRP-A contigs based on their homology to <i>T. pseudonana</i> and <i>P.</i>
(Kellogg et al. 2022a), To further support this inference, we used SHOOT (Emms and Kelly	tricornutum ZCRP-A proteins, which we have previously characterized as Zn-responsive
	(Kellogg et al. 2022a), To further support this inference, we used SHOOT (Emms and Kelly

2022) to place each ZCRP-A contig within a phylogenetic context. Of the 21 unique contigs

Formatted: Font: Italic

assigned as ZCRP-A homologs, 19 were confirmed to be T. pseudonana orthologs, while 2 were assigned as orthologs to the Zn-related COG0523 E. coli proteins YjiA and YeiR, implying a minor prokaryotic source (Supplementary Table 5). The placement of the majority of these contigs within diatom clades supports our interpretation that these homologs are Zn-related. ZIP proteins were almost solely detected in the 51 µm fraction, likely due to the capture of abundant Phaeocystis colonies and chain-forming diatoms (Fig. 3e; Supplementary Figure 5c). ZIP family transporters are functionally diverse and capable of transporting multiple divalent metal cations, including both Zn2+ and Fe2+ (Blaby-Haas and Merchant 2012), with diatom homologs of ZIP1 known to be upregulated under Fe stress (Lampe et al. 2018). Given the co-limitation of Fe and Zn at the study site, it is difficult to determine which metal these ZIP transporters were primarily mediating. The increased abundance of diatom θ -CA and δ -CA proteins within the water column (Fig. 3f,g), as well as transcripts for the diatom Cd carbonic anhydrase CDCA, which can replace Zn²⁺ with Cd²⁺ as the catalytic cofactor (Lane and Morel 2000a), in the 3 μm and 51 μm fractions at 200 m (Fig. 3h) was indicative of a sinking, prior diatom bloom event (Subhas et al. 2019). θ-CA and δ-CA were predominantly taxonomically assigned to the diatom genera Chaetoceros and Pseudo-nitzschia, respectively, while CDCA transcripts belonged to the diatom genera Chaetoceros and Corethron (Fig. 3i). The presence of θ -CA, but lack of δ -CA, assigned to Chaetoceros is consistent with proteomic analysis of the polar diatom Chaetoceros neogracile RS19 grown in culture under Zn limiting conditions (Kellogg et al. 2022b).

2.6 Zn:P ratios of the surface seawater at the experimental site

299

300

301

302

303

304

305

306

307

308

309

310

311

312

313

314

315

316

317

318

319

320

Formatted: Font: Italic
Formatted: Font: Italic
Formatted: Font: Italic
Formatted: Font: Bold

Formatted: Superscript
Formatted: Superscript

A third independent line of evidence for the nutritional influence of Zn scarcity on TNB phytoplankton was obtained from *in situ* cellular stoichiometry. Particulate Zn:P ratios (Zn:P) analyzed from biomass collected at the surface of this experimental station were consistent with ratios from Zn-limited culture studies. Particulate Zn:C ratios reported previously in Zn-limiting culture studies of the diatom *Thalassiosira pseudonana* (Sunda and Huntsman 2005) were converted to Zn:P ratios using the Redfield ratio (Redfield 1958) (Supplementary Table 65). We then compared these ratios and associated growth rates with particulate Zn:P measured within biomass collected at 10, 25, 50 and 100 m at the experimental site. At each of these surface depths, Zn:P measured at the experimental site was ~ 2E-4 mol:mol, which, in comparison to cultured diatom Zn:P ratios, fell within the range of severely Zn-limited growth rates (Supplementary Figure 6), again demonstrating the propensity for Zn-limited growth in this region and corroborating the incubation results.

3 Discussion

Antarctic waters are generally considered to not be prone to Zn limitation, given that high (> 1nM) dZn concentrations are typically observed in surface Southern Ocean waters (Coale et al. 2003). -However, we observed multiple independent lines of evidence from both the field incubation experiment (chlorophyll, DIC, Zn and Fe biomarker proteins) and contextual environmental biogeochemical data of the water column at the incubation site (dZn, Zn uptake rates, pigments, cellular Zn:P stoichiometry, metaproteomic, and metatranscriptomic analyses) demonstrating that phytoplankton within Terra Nova Bay of the Ross Sea, Antarctica, were experiencing Zn and Fe nutritional stress.

Multiple factors could be considered as potential drivers in the creation of Zn-limiting conditions in the field, including Zn demand imposed by total biomass and the species comprising this biomass. The phytoplankton bloom observed during this expedition was comprised primarily of diatoms and *Phaeocystis*, consistent with previous Ross Sea seasonal blooms (Smith et al. 2006; Arrigo et al. 2012; Mangoni et al. 2019), and which contributed to the observed high Zn uptake rates and thus surface Zn depletion (Kell et al. 2024), resulting in nutrient-like dZn profiles throughout TNB.

Our field observation of Zn limitation was made in an environment characterized by diminished pCO₂, which we consider as a factor potentially driving Zn stress. We observed a substantial drawdown of surface seawater pCO₂ to 221 µatm at the incubation site (a ~45% decrease compared to offshore waters in the Ross Sea measured during the same time frame; Fig. 1b). Biology was the driver of this decrease in pCO₂, rather than freshwater input from glacial and sea ice melt. This is evident in the physicochemical data, where over the measured salinity range (S=33.6-34.8), the effect of simple dilution by freshwater input (DIC=Total Alkalinity=0) would result in a reduction of pCO₂ by only ~8-9 ppm. The signals we observe are much larger than that, consistent with a large phytoplankton uptake driver. The total alkalinity (TA) also does not change proportionally with DIC in this region, which is also not consistent with dilution driving a conservative mixing of TA and DIC.

Laboratory studies have unequivocally demonstrated that marine phytoplankton can easily be Zn-limited in culture due to their large Zn requirement, and that this effect is exacerbated at low pCO₂ (Morel et al. 1994; Sunda and Huntsman 2005) due to the use of Zn as a required catalytic cofactor within carbonic anhydrase (CA) metalloenzymes (Sunda and Huntsman 2005). CAs catalyze the reversible dehydration of HCO₃⁻ to CO₂, the substrate

Formatted: Subscript

Formatted: Subscript

required by the carbon fixing enzyme RUBISCO. As HCO₃⁻ constitutes about 90% of the dissolved inorganic carbon (DIC) pool in the surface ocean, sufficient CA activity prevents carbon stress in marine phytoplankton by ensuring adequate CO₂ supply to RUBISCO. It has therefore been hypothesized that the combination of high biomass and resulting low CO₂ may cause severe Zn depletion that may limit algal growth rates due to lack of Zn and thus reduced CA activity, and thus reduced availability of carbon for photosynthesis (Morel et al. 1994; Sunda and Huntsman 2005). This Zn-C limitation relationship is referred to as 'biochemically dependent co-limitation', in which the availability of one nutrient is essential for the acquisition or utilization of another nutrient, especially at low concentrations (Saito et al. 2008).

To explore this in the context of our field observations, using the available quantitative constraints on Zn and CO₂ co-limitation thresholds available from the literature (see Methods), we estimated that the threshold for Zn-CO₂ limitation in culture synthesized across many alga occurs at 259 μ atm pCO₂. We then compared this laboratory-determined Zn/C limitation threshold estimate to both the *in situ* 221 μ atm pCO₂ measured at our field study site, and to the historical, global trend in surface ocean pCO₂ (Fig. 4a,b). Global surface ocean pCO₂ levels are rapidly rising above both the laboratory-estimated 259 μ atm pCO₂ Zn/C limitation threshold and our field observation value of 221 μ atm (Jiang et al. 2023) (Fig. 4a,b). Though only a fraction of the modern-day surface ocean is currently at \leq 250 ppm pCO₂ (predominantly comprised of polar regions; Fig. 4c), this represents a large decrease in oceanic extent compared to only 100 years ago (Fig. 4d). Even though this may move the majority of oceanic regions farther from Zn and C limitation thresholds, there continue to be highly productive and episodic coastal blooming events that induce significant pCO₂ drawdown (Harrison et al. 2018; Dai et al. 2022). These coastal regions are increasingly recognized as being disproportionally significant contributors to

global ocean carbon export (with respect to their area), particularly at the high latitudes (Harrison et al. 2018; Dai et al. 2022), and will hence continue to be prone to Zn stress at low CO₂ as we have observed. Many other coastal regions have been observed to experience depressed CO₂ such as the Amundsen Sea (Tortell et al. 2012), Amazon River plume (Valerio et al. 2021), the west Florida Shelf (Robbins et al. 2018), the East China Sea (Shim et al. 2007), the Northern Gotland Sea (Schneider and Müller 2018), and Monterey Bay, California (Chavez et al. 2018) to name a few examples. On the other hand, it is likely that despite rising pCO₂ levels, some coastal regions will continue to experience episodic or persistent low pCO₂ due to high productivity (as observed in this study), freshwater inputs, or other regional processes. Though we do not attempt to model future pCO₂ dynamics in these areas, our results suggest that Zn status may continue to be an important physiological constraint under low pCO₂ conditions, particularly in productive coastal systems. As such, Zn limitation should be considered as part of the broader framework for understanding carbon cycling in these regions, especially as they play a disproportionate role in global carbon export.

4 Conclusions

Given the great challenge of conducting Zn manipulation experiments without contamination, we did not try to manipulate pCO₂ as an additional experimental treatment. Instead, we actively sought out a low pCO₂ environment for the study site, building on prior laboratory studies and a cadmium (Cd) pCO₂ field study (Cullen et al. 1999). The interaction of Zn (and Cd and Co) with CO₂ is an important area of future research, particularly in coastal environments. With the continuing rise in atmospheric and surface ocean pCO₂ levels, broader changes in the biogeochemical cycling of Zn and other bioavailable trace metals will likely occur

within the oceans, influencing NPP and thus total ocean carbon storage capacity. These low pCO₂ conditions environments that routinely occur in numerous coastal environments globally should be further examined for Zn effects in addition to carbon uptake dynamics in different temperature environments (Tortell et al. 2008; Dai et al. 2022). While there are elaborate biochemical capabilities available to many marine algae for dealing with Zn scarcity (Kellogg et al. 2022a), our results suggest that the geographic extent of possible Zn/C co-limiting environments may further decrease in the coming decades with rising anthropogenic CO₂ emissions. Despite this, the biochemical demand for Zn in marine organisms remains substantial, with cellular demand rivaling that of Fe. The multitude of metabolic functions requiring Zn, including but not limited to carbonic anhydrase activity, implies the need for further exploration of Zn influences on primary productivity in a changing ocean environment.

5 Materials and Methods

5.1 Study area and sample collection

Sample collection occurred during the CICLOPS (Cobalamin and Iron Co-limitation of Phytoplankton Species) expedition (NBP18-01) aboard the RVIB *Nathaniel B. Palmer*,

December 11, 2017 – March 3, 2018 in the Amundsen Sea and Ross Sea of the Southern Ocean (Fig. 1a). Station metadata is provided in Supplementary Table 2. All stations were assumed to be representative of TNB during this temporal study (as evident in the total dissolved metal, macronutrient, and chlorophyll *a* datasets). Water samples for dissolved trace metal analyses were collected using trace metal sampling protocols described previously (Cutter and Bruland 2012). A trace metal clean rosette suspended on a Kevlar line and equipped with twelve 8L X-Niskin bottles (Ocean Test Equipment) was used to collect seawater at depths ranging from 10 –

600 m. Niskin bottles were transported to a positive-pressure trace metal clean shipboard van for filtration upon surfacing. Total fluorescence on the vertical profiles was measured using an ECO chlorophyll fluorometer (Wet Labs) equipped to the rosette. The rosette also included instrumentation for measuring conductivity and temperature (Sea-Bird Electronics).

5.2 Preparation of plasticware

Polyethylene and polycarbonate sampling and incubation bottles were rigorously cleaned to remove trace metal contaminants before use. Bottles were rinsed with 18.2 Ω Milli-Q water (Millipore), soaked for 72h in <1% Citranox detergent, rotated, soaked for an additional 72h, and then rinsed five times with Milli-Q water. Bottles were then filled with 10% HCl (Baker instaranalyzed) by volume and soaked for a minimum of one week, rotated, and soaked for another week. Bottles were then rinsed five times with dilute acid (HCl, pH 2) and stored double-bagged in plastic zip bags. All cleaning work was conducted in a Class 100 clean room.

5.3 Underway seawater pCO₂ partial pressure

Surface water pCO₂ measurements were conducted aboard the RVIB *Nathaniel B*.

Palmer using an underway method consisting of an air-water equilibrator and IR CO₂ analyzer developed and operated by the Lamont-Doherty Earth Observatory (LDEO) group (Takahashi et al. 2020). A complete data report and sensor list are available: https://service.rvdata.us/data/cruise/NBP1801/doc/NBP1801DATA.pdf (last access: 14 December 2024).

5.4 TDIC and POC measurements

Total alkalinity (TA) and dissolved inorganic carbon (DIC) were measured on CTD and incubations samples in near real-time aboard the NBP. Dissolved inorganic carbon (DIC) and total alkalinity (TA) samples were collected following previously establishedthe protocols-of Dickson et. al 2007 (Dickson et al. 2007). DIC analyses were conducted within ~4 h of collection. We acidified 1.25 mL of sample using an automated custom-built injection and bubble stripping system coupled to an infrared gas analyzer (LICOR LI7000) and integrated the infrared absorption signal versus time for each stripped gas sample to yield a total mass of CO₂. Each sample was analyzed in triplicate or greater. Since microbubbles regularly formed as samples warmed between sample acquisition and DIC analysis, every integration curve was visually inspected and those curves that exhibited evidence for bubbles were rejected. Certified reference materials (Dickson CRM batch 169) were analyzed between every 3 to 4 unknowns. The estimated precision based upon unknowns (>860 samples run in triplicate) and CRM replicates (n = 738) was ± 2.0 μ mol kg⁻¹ (± 1 SD). As described by DeJong et al. 2015(DeJong et al. 2015), Aanalyses for TA on filtered samples were completed within ~12 h of collection by using a potentiometric titrator (Metrohm 855 Robotic Titrosampler) (DeJong et al. 2015). The estimated precision based on replicate analyses of CRMs (n = 195) was \pm 2.6 μ mol kg⁻¹ (\pm 1 SD).

5.5 Analysis of historical atmospheric and surface ocean pCO2 trends

458

459

460

461

462

463

464

465

466

467

468

469

470

471

472

473

474

475

476

477

478

479

480

Decadal surface ocean pCO₂ reconstructions from Jiang et al. 2023 (Jiang et al. 2023) were downloaded, binned by decade, and plotted using the 'violinplot' in MATLAB.

Atmospheric pCO₂ data was assembled from the running Mauna Loa record (Keeling et al. 1976), and from measurements made on Antarctic firn ice (Etheridge et al. 1996).

5.6 Calculation of Zn-and pCO₂ co-limitation of phytoplankton thresholds

There are few experimental measurements of Zn- and pCO₂-co-limitation, either in the lab or *in situ*. This study documented Zn of a natural phytoplankton assemblage in the field at a pCO₂ of ~220 ppm. In the literature, several models exist to interpret co-limitation (Buitenhuis et al. 2003; Saito et al. 2008). For this study we chose to use the biochemically dependent co-limitation model for growth rate (μ):

$$\mu = V_{max} \frac{\left[CO_{2(aq)}\right]}{\varphi K_s + \left[CO_{2(aq)}\right]}, \quad (1)$$

where V_{max} is the maximum growth rate, $[CO_{2(aq)}]$ is the aqueous CO_2 concentration of the growth medium in micromoles per kilogram of seawater, K_s is the half-saturation constant in micromoles per kilogram of seawater, and φ is a Zn-dependent growth term:

$$\varphi = \frac{[dZn] + K_{s,Zn}}{[dZn]} \tag{2}$$

Here, the dissolved Zn concentration in the growth medium [dZn] is modified by a Zn-dependent saturation constant ($K_{s,Zn}$). Few studies have enough experimental data to robustly establish a kinetic relationship between [dZn] and [CO_{2(aq)}], so we compiled several estimates for these terms from the literature. Diatom growth rates under pCO₂ limitation were taken from Riebesell et al. (1993) (Riebesell et al. 1993). Reported pH and temperature measurements for each treatment, a total alkalinity of 2300 µmol kg⁻¹, and a salinity of 35 were used to calculate aqueous CO₂ concentrations using CO2SYSv3.2.1.(Sharp et al. 2023). Reported V_{max} and K_s for D. brightwellii, T. punctigera, and R. alata were 1.46, 1.30, and 0.93 d⁻¹, and 1.4, 1.2, and 2.1 µmol kg⁻¹, respectively. Values for coccolithophore growth ($K_s = 0.97$ µmol kg⁻¹, $V_{max} = 4.7$ d⁻¹) were taken from Krumhardt et al. (2017) (Krumhardt et al. 2017). A value for $K_{s,Zn}$ of 300 pmol

L⁻¹ was taken from Buitenhuis et al. (2003). This value is for the coccolithophore E. huxleyii generated under varying CO₂ and Zn conditions, and Zn response growth curves under single CO₂ conditions (ambient) are similar to other diatoms like T. pseudonana (Sunda and Huntsman 1995). The value of 300 pmol L⁻¹ appears high, but is tied to the functional form of the biochemically co-limitation equation (Buitenhuis et al. 2003; Saito et al. 2008). Based on the same dataset and different models for co-limitation, Buitenhuis et al. (2003) arrived at $K_{s,Zn}$ values of ranging from 38 pmol L⁻¹ to 300 pmol L⁻¹. They calculated Zn-limitation alone, at CO₂replete conditions, of 19 pmol L⁻¹. Thus, the chosen value of $K_{s,Zn}$ is not a reflection of high Zn demand but determined by the functionality of biochemical co-limitation by Zn and C. To calculate φ, a surface ocean Zn concentration of 50 pmol L⁻¹ was assumed (Bruland 1980; Wyatt et al. 2014). While these concentrations reflect total dissolved Zn, the relationship between bioavailable free Zn and dZn, especially in the field, remains unclear. Eq. 1 was then used to calculate effective CO2 concentrations (and thus pCO2 values) at which growth is halved, or in other words, $\mu = 0.5 V_{max}$. We note that this calculation is distinct from the CO₂ halfsaturation constant because of the co-limitation by Zn. The median pCO₂ threshold for 50% growth from the three diatom species was 278 ppm. Including coccolithophores decreases the median to 259 ppm. These values are slightly higher than the in situ evidence for Zn limitation at 220 ppm presented in the present study. Our results cannot be considered as an upper bound for Zn-CO₂ limitation, but serve as evidence for growth limitation under those specific environmental conditions.

521522

523

502

503

504

505

506

507

508

509

510

511

512

513

514

515

516

517

518

519

520

5.7 Analyses of total dissolved metals using isotope dilution

The analysis of total dissolved metals for this expedition has been described previously (Kell et al. 2024). Briefly, seawater collected shipboard by pressure-filtering X-Niskin bottles through an acid-washed 142 mm, 0.2 µmM polyethersulfone Supor membrane filter (Pall) within 3 hours of rosette recovery using high purity (99.999%) N₂ gas and stored at 4°C. All sample collection occurred shipboard within an on-deck trace metal clean van. Samples were acidified to pH 1.7 with high purity HCl (Optima) within 7 months of collection and were stored acidified at room temperature for over 1 year prior to analysis. This extended acidification time was used to counteract any loss of metal due to adsorption to the bottle walls (Jensen et al. 2020b), Quantification of total dissolved Fe, Mn, Ni, Cu, Zn, and Cd was performed using isotope dilution. Acidified seawater samples were spiked with a stable isotope spike solution artificially enriched in ⁵⁷Fe, ⁶¹Ni, ⁶⁵Cu, ⁶⁷Zn, and ¹¹⁰Cd (Oak Ridge National Laboratory). Concentrations and spike ratios were verified by ICP-MS using a multi-element standard curve (SPEX CertiPrep). Preconcentration of spiked seawater samples for total dissolved metal analysis was performed using the automated solid phase extraction system seaFAST-pico (Elemental Scientific) in offline concentration mode with an initial volume of 15mL and elution volume of 500µL (Rapp et al. 2017; Wuttig et al. 2019). Following preconcentration, multielemental quantitative analysis was performed using an iCAP-Q inductively coupled plasma-mass spectrometer (ICP-MS) (Thermo Scientific). Concentrations of Mn, Fe, Ni, Cu, Zn and Cd were determined using a six-point external standard curve of a multi-element standard (SPEX CertiPrep), diluted to range from 1-10 ppb in 5% nitric acid. An indium standard (SPEX CertiPrep) was similarly added to these standard stocks, diluted to range 1-10 ppb. Instrument injection blanks consisted of 5% nitric acid in Milli-O. Standard curve R² values were ≥0.98 for

all metals monitored. Method accuracy and precision were assessed using the 2009

524

525

526

527

528

529

530

531

532

533

534

535

536

537

538

539

540

541

542

543

544

545

GEOTRACES coastal surface seawater (GSC) standard (n = 8; **Supplementary Table 76**), which produced values consistent with consensus results (Kell et al. 2024).

5.8 Macronutrient, pigment, and Fv/Fm analyses

Seawater for macronutrient (silicate, phosphate, nitrate, and nitrite) analyses were filtered through 0.2 µm pore-size Supor membrane filters and frozen at sea in acid-washed 60-mL high-density polyethylene bottles until analysis. Macronutrient analyses were conducted by nutrient autoanalyzer (Technicon Autoanalyzer II) by Joe Jennings at Oregon State University. The chemotaxonomic distribution of phytoplankton pigments was determined using HPLC as described previously (DiTullio et al. 2003). Photosynthetic efficiency of photosystem II (Fv/Fm) was measured using a Phyto PAM phytoplankton analyzer (Walz, Effeltrich, Germany) as described previously (Schanke et al. 2021).

5.9 Bacterial abundance

One ml samples for heterotrophic prokaryotes abundance (HPA) analysis were fixed for 10 min with a mix of paraformaldehyde and glutaraldehyde (1% and 0.05% final concentration, respectively), frozen in liquid nitrogen and stored at –80°C until analysis. After thawing, samples were stained with SYBR Green (Invitrogen Milan, Italy) using 10⁻³ dilution of stock solution for 15 min at room temperature. Cell concentrations were assessed using a FACSVerse flow cytometer (BD BioSciences Inc., Franklin Lakes, USA) equipped with a 488 nm Ar laser and standard set of optical filters. FCS Express software was used for analyzing the data and HP were discriminated from other particles on the basis of scatter and green fluorescence from SYBR Green (Balestra et al. 2011).

5.10 ICP-MS analysis and Zn uptake rates using ⁶⁷Zn

570

571

572

573

574

575

576

577

578

579

580

581

582

583

584

585

586

587

588

589

590

591

592

⁶⁷Zn stable isotope uptake experiments were performed to quantify the movement of dissolved Zn to the particulate phase (in units of pmol L⁻¹ d⁻¹), see (Kell et al. 2024). Briefly, unfiltered seawater was collected using the trace metal rosette over a depth range of 10-600 m into 250mL trace metal clean polycarbonate bottles. Bottles were spiked with ⁶⁷Zn such that the total added (spiked) concentration of Zn was 2 nM. Immediately after spiking, incubation bottles were sealed, inverted to mix, and transferred to flow-through on-deck incubators for 24hr. Biomass was collected after 24hr by vacuum filtering each incubation sample at 34.5 kPa (5 psi) onto an acid-cleaned 3µm pore-size acrylic copolymer Versapore filter (Pall) mounted on an acid-cleaned plastic filtration rig. Sample filters were retrieved from storage at -80°C, removed from cryovials using plastic acid-washed forceps, and transferred into trace metal clean 15 mL PFA vials with 4 mL of 5% HNO₃ (Optima) containing a 1 ppb Indium (In) internal standard. Filters were digested for ~3.5h at 140°C using a HotBlock® heating block (Environmental Express, USA) before they were removed and discarded. After evaporating the remaining solution to just dryness, the residue was resuspended in 2 mL of 5% HNO₃ (Optima) by light vortexing. Process blank filters were digested and processed as sample filters were. This experiment was also carried out using 110Cd as a tracer of Cd uptake in separate incubation bottles (data not shown here). Digests were analyzed in duplicate by ICP-MS using a Thermo ICAP-Q plasma mass spectrometer calibrated to a multi-element standard curve (Spex Certiprep) over a range of 1 – 20 ppb. Natural Cd and Zn isotope abundances of the standards were assumed to calculate concentrations of 110Cd, 111Cd, 114Cd, 67Zn, 66Zn, and 68Zn. Total Zn uptake (pmol L⁻¹ d⁻¹) was calculated using particulate ⁶⁷Zn and total water column dZn measurements as

described previously_(Cox et al. 2014). The particulate metal measurements captured contributions from the active transport of metal into cells, nonspecific metal adsorption to cell surfaces, metal adsorption to non-living particulate organic matter, and metal adsorption to particulate inorganic matter, though we expect active transport into cells to dominate the measured particulate isotopic signal due to the high abundance of actively growing autotrophic cells in the photic zone observed in Southern Ocean during austral summer. Particulate Zn:P measurements were calculated using particulate Zn measured on Cd-spiked filters and thus do not include any pZn contribution from Zn tracer addition. Particulate phosphorus concentrations were measured by ICP-MS simultaneously and were calibrated to a standard curve ranging from 100 to 3200 ppb using a 1 ppm certified P stock (Alfa Aesar Specpure). All SPEX and P standard curves had R² values > 0.99. The Zn stock solution used in the incubation experiments was similarly analyzed by ICP-MS to confirm that the stock was not Fe contaminated—this analysis showed that less than 2.3 pM (which was near the instrument blank level for this analysis) of iron was added for every 2 nM of zinc, far less than needed to stimulate phytoplankton to the extent observed in our experiments.

5.11 Shipboard incubation experiments

Incubation experiments were conducted at station 27 (-74.9870°N, 165.8898°E). Raw surface seawater was pumped directly into a cleanroom container van, collected into acid-cleaned 50L carboys, and dispensed into acid-washed 1L polycarbonate bottles using a trace metal sampling system with acid-washed polypropylene tubing and a teflon diaphragm pump. Incubation bottles were first rinsed with seawater then filled. Seawater was collected at 16:05 UTC. Triplicate incubation bottles were amended with +Fe (1 nM), +Zn (2 nM) and +Fe+Zn,

sealed, and placed into a flow-through on-deck incubator with light screens that shaded the incubator to 20% percent ambient surface irradiance. Incubations were sampled at 0, 48, 96, and 144 hours (corresponding to T0, T2, T4, and T6 timepoints) for analysis by filtering onto GFF filters for chlorophyll (all time points, biological triplicates), pigment analyses (T6, biological triplicates), and proteomic analyses (T6, pooled biological triplicates). Chlorophyll was extracted immediately, otherwise samples were frozen at -80°C until further analyses, with pigment and protein samples kept in -80°C freezers, liquid nitrogen dewars, or dry ice coolers at all times during transport back to the laboratories. All amendments and sampling were conducted in a positive-pressure, clean room van with laminar flow hoods and plastic sheeting to minimize trace-metal contamination.

5.12 Metaproteomic analysis

Water column metaproteomic biomass was collected onto 0.2, 3, and 51 μm pore-size filters ("field filters") using in-situ battery operated McLane pumps. Half of each field filter was processed for metaproteomic analysis. Incubation metaproteomic biomasssamples wasere serially filtered through a 5μm pore prefilter followed by a 142mm GFF filter. Three-fourths of each GFF filter was used for subsequent metaproteomic analysis of the incubations. All filters were frozen at -80°C and stored until laboratory extraction. To extract proteins, filters were placed into extraction buffer (1% SDS, 0.1M Tris/HCL pH 7.5, 10mM EDTA). 8 mL of buffer was used for each field filter, and 15 mL of buffer was used for each GFF incubation filter. All reagents were made with HPLC-grade water. Samples were heated at 95°C for 10 minutes and shaken at room temperature for 30 minutes. Filters were removed and protein extracts were filtered through 5.0 μm Millex low protein binding filters (Merck Millipore #SLSV025LS).

Millex filters were rinsed with 1 mL of extraction buffer to ensure no loss of protein. Samples were then spun for 30 minutes at 3220 rcf in an Eppendorf 5810 centrifuge. The supernatant was transferred to Vivaspin 5K MWCO ultrafiltration columns (Sartorius #VS0611). Protein extracts were concentrated to approximately 300 μL, washed with 1 mL of extraction buffer, and transferred to a 2 mL ethanol-washed microtube (all tubes from this point on are ethanol-washed). Vivaspin columns were rinsed with small volumes of protein extraction buffer to remove all concentrated protein and samples were brought up to 400 μL with extraction buffer. Samples were incubated with 2 μL benzonase nuclease (EMD Millipore 70746-3) for 30 minutes at 37°C.

Extracted proteins were purified from SDS detergent, reduced, alkylated and digested

with trypsin while embedded within a polyacrylamide tube gel, using a modified, previously published method (Lu and Zhu 2005). A gel premix was made by combining 1 M Tris HCL (pH 7.5) and 40% Bis-acrylamide L 29:1 (Acros Organics) at a ratio of 1:3. The premix (103 μL) was combined with 50-100 μg of the extracted protein sample, Tris-EDTA, 7 μL 1% APS and 3 μL of TEMED (Acros Organics) to a final volume of 200 μL. After 1 hour of polymerization at room temperature, 200 μL of gel fix solution (50% ETOH, 10% acetic acid in LC/MS grade water) was added to the top of the gel and incubated at room temperature for 20 minutes. Liquid was then removed and the tube gel was transferred into a new 1.5 mL microtube containing 1.2 mL of gel fix solution before incubating at room temperature, 350 rpm in a Thermomixer R (Eppendorf) for 1 h. Gel fix solution was removed and replaced with 1.2 mL of destain solution (50% MeOH, 10% acetic acid in LC/MS grade water) and incubated at 350 rpm, room temperature for 2 h. Liquid was removed, gels were cut up into 1 mm cubes and added back to tubes containing 1 mL of 50:50 acetonitrile:25 mM ammonium bicarbonate (ambic) and

Formatted: Indent: First line: 0.5"

incubated for 1 h, 350 rpm at room temperature. Liquid was removed and replaced with fresh
50:50 acetonitrile:ambic solution and incubated at 16°C, 350 rpm overnight. The above step was
repeated for 1 hour the following morning. Gel pieces were then dehydrated twice in 800 μl of
acetonitrile for 10 min at room temperature and dried for 10 min in a ThermoSavant DNA110
speedvac after removing the solvent. Proteins were reduced in $600~\mu L$ of $10~mM$ DTT, $25~mM$
ambic at 56°C, 350 rpm for 1 h. The volume of unabsorbed DTT solution was measured prior to
removal. Gel pieces were washed with 25 mM ambic, and 600 μL of 55 mM iodoacetamide was
added to alkylate proteins at RT, 350 rpm for 1 h. Gel cubes were then washed with 1 mL ambic
for 20 minutes, 350 rpm at RT. Acetonitrile (1mL) dehydrations and speedvac drying were
repeated as described above. Trypsin (Promega #V5280) was added in an appropriate volume of
25 mM ambic to rehydrate and submerse gel pieces at a concentration of 1:20 μg trypsin:protein.
Proteins were digested overnight at 350 rpm, 37°C. Unabsorbed solution was removed and
transferred to a new tube. 50 μ l of peptide extraction buffer (50% acetonitrile, 5% formic acid in
water) was added to gels, incubated for 20 min at RT, then centrifuged at 14,100 x g for 2 min.
The supernatant was collected and combined with the corresponding unabsorbed solution. The
above peptide extraction step was repeated again, combining corresponding supernatants.
Combined digested peptides were centrifuged at 14,100 x g for 20 minutes, supernatants
transferred into a new tube and dehydrated down to approximately 20 μL in the speedvac. Total
digested peptides were quantified (Bio-Rad DC protein assay, Hercules, CA) with BSA as a
standard. Peptides were then diluted in 2% acetonitrile, 0.1% formic acid in LC/MS grade water
to a concentration of $1\mu g/\mu L$ for storage until analysis. All water used in the tube gel digestion
protocol was LC/MS grade, and all plastic microtubes were ethanol rinsed and dried prior to use.

Purified peptides were diluted to $0.1~\mu g~\mu l^{-1}$ and $20~\mu l~(2~\mu g)$ was injected onto a Dionex UltiMate 3000 RSLCnano LC system (Thermo Fisher Scientific) with an additional RSLCnano pump run in online two-dimensional active modulation mode coupled to a Thermo Fusion Orbitrap mass spectrometer as described previously (McIlvin and Saito 2021).

Frozen filters were thawed and extracted as described previously (Hughes et al. 2014). Briefly, filters were extracted using SDS detergent to solubilize both membrane and soluble proteins and subjected to a 10-min heating incubation at 95°C. Protein material was subsequently purified, alkylated, reduced and digested with trypsin (mass spectrometry grade; Promega Corporation) at a trypsin:protein ratio of 1:20 and peptides were purified using C18 tips (Pierce C18 Tips, 100-μl bed; Thermo Fisher Scientific). Purified peptides were diluted to 0.1 μg μl=1 and 20 μl (2 μg) was injected onto a Dionex UltiMate 3000 RSLCnano LC system (Thermo Fisher Scientific) with an additional RSLCnano pump run in online two dimensional active modulation mode coupled to a Thermo Fusion Orbitrap mass spectrometer.

A translated metatranscriptome (see below) was used as a reference protein database and peptide spectra matches were performed using the SEQUEST algorithm within Proteome Discoverer v.2.1 (Thermo Fisher Scientific) with a fragment tolerance of 0.6 Da and parent tolerance of 10 ppm. Identification criteria consisted of a peptide threshold of 95% (false discovery rate (FDR) = 0.1%) and protein threshold of 99% (1 peptide minimum, FDR = 0.8%) in Scaffold v.5 (Proteome Software) resulting in 5,387 proteins identified in the incubation experiment and 27,924 proteins identified in the water column. To avoid double-counting mass spectra, exclusive spectral counts were used for the downstream proteomic analysis. Exclusive spectral counts were normalized using the normalized spectral abundance factor (NSAF) calculation (Zhang et al. 2010) to allow for a comparison of protein abundance across samples

while remaining consistent with the metatranscriptomic procedure, see Cohen et al. 2021 for details. Counts associated with redundant ORFs (sharing identical taxonomic and functional assignments) were summed together. The stand-alone command line application BLAST+ from the National Center for Biotechnology Information (NCBI) was used to identify proteins of interest in the metaproteomic data. Metaproteomes were BLAST searched (E = 5e-5) against the known sequences of proteins of interest acquired from annotated proteomic databases (Supplementary Table 4) and combined with further annotation data based on contig ID (see below).

5.13 Metatranscriptomic analysis

RNA sequencing was performed using the Illumina HiSeq platform. Transcriptomic assemblies were generated for biomass collected using McLane pumps filtered through 0.2, 3, and 51 µm pore-size filters. In order to enrich metatranscriptomic libraries derived from 0.2 µm filters in prokaryotic transcripts and libraries derived from 3 µm and 51 µm filters in eukaryotic transcripts, 0.2 µm libraries were generated from total rRNA-depleted mRNA and 3 µm and 51 µm libraries were generated from polyA mRNA. Total RNA was extracted from 0.2 µm, 3 µm, and 51µm filters using Macherey-Nagel a NucleoMag RNA kit (Macherey-Nagel GmbH & Co.KG). Cleared lysate was loaded into a 96 deep-well plate and put on an epMotion 5075 TMX liquid handler to complete the RNA extraction following the Machery-Nagel standard protocol. For 3 µm and 51 µm samples with total RNA greater than 1 µg, 800 ng of total RNA was used for preparing poly A libraries with an Illumina Stranded mRNA Prep Ligation kit (Illumina), following the manufacturer's protocol. For the 3 µm and 51 µm samples with total RNA less than 1 µg, 20 ng of total RNA was used as input for the SMART-Seq v4 Ultra Low Input RNA

kit (Takara Bio USA. Inc), which converts poly(A) RNA to full-length cDNA using a modified oligo (dT) primer with simultaneous cDNA amplification. The resulting double-stranded cDNA was then fragmented using a Covaris E210 system with the target size of 300bp. Libraries were prepared from fragmented double-stranded cDNA using an Illumina Stranded mRNA Prep Ligation kit (Illumina). For RNA obtained from 0.2 µm filters, ribosomal RNA was removed using a riboPOOL Seawater Kit (Galen Laboratory Supplies, North Haven, Connecticut, USA). The riboPOOL Seawater Kit is a customized mixture of Removal Solutions: Pan-Prokaryote riboPOOL, Pan-Plant riboPOOL and Pan-Mammal in a ratio of 6:1:1. The rRNA-depleted total RNA was used for cDNA synthesis by Ovation RNA-Seq System V2 (TECAN, Redwood City, USA). Double stranded cDNA was then prepared for the libraries using an Illumina Stranded mRNA Prep Ligation kit (Illumina). Ampure XP beads (Beckman Coulter) were used for final library purification. Library quality was analyzed on a 2200 TapeStation System with an Agilent High Sensitivity DNA 1000 ScreenTape System (Agilent Technologies, Santa Clara, CA, USA). Resulting libraries were subjected to paired-end Illumina sequencing via NovaSeq S4. The input paired-end fastq sequences are trimmed of sequencing adapters, primers and low quality bases by using either BLASTN (NCBI, v2.2.25) (Altschul et al. 1990) or trimmomatic, v0.36 (Bolger et al. 2014). The trimmed paired and unpaired sequences were then depleted of rRNA sequences with riboPicker v0.4.3 (Schmieder et al. 2012). The command-line program clc assembler, v5.2.1 (Qiagen) was used to assemble processed sequences into contigs and ORFs were identified by FragGeneScan, v1.31 (Rho et al. 2010). The trimmed sequences were mapped to the predicted ORFs using the command-line program clc mapper, v5.2.1 (Qiagen) to generate mapped raw read counts for each ORF. The raw counts were normalized initially to RPKM values, to account for variations in inter-sample sequencing depth and the

730

731

732

733

734

735

736

737

738

739

740

741

742

743

744

745

746

747

748

749

750

751

ORF sequence length (Mortazavi et al. 2008). The RPKM values were subsequently converted to TPM (transcripts per million) units for estimation of the relative RNA abundance among samples (Li and Dewey 2011). The ORFs were annotated for putative function by several programs in parallel using BLASTP against PhyloDB, hidden Markov models PFAM and TIGRFAM by HMMER, v3.3.2 (Eddy 2011), KEGG Ortholog HMM by kofamscan, v1.3.0 (Aramaki et al. 2020), and transmembrane HMM by TMHMM (Krogh et al. 2001). Additional annotations were generated by similarity searches using BLASTP to transporter (PhyloDB), organelle (PhyloDB) and KOG (Tatusov et al. 2003) databases. The ORFs are assigned to the best taxonomic species/group as determined by LPI (Lineage Probability Index) analysis (Podell and Gaasterland 2007). The final list of curated ORFs was generated by removing ORFs with low mapping coverage (< 50 reads total over all samples) and with no BLAST hits and no known domains.

5.14 Statistical analysis and data visualization

ANOVA and Dunnett tests were performed using MATLAB 2019a. Statistics are summarized in **Supplementary Table 3**. Figures were made using matplotlib (version 3.5.0), Ocean Data View (version 5.5.2), Excel (2019), and RStudio (version 1.3.1093). Color palettes used in Ocean Data View section plots (https://doi.org/10.5281/zenodo.1243862) are inverse "roma" for trace metal concentrations, "thermal" for Zn and Cd uptake rates, and "algae" for chlorophyll fluorescence (Crameri 2023).

Data Availability

775	CICLOPS (NBP18-01) conductivity-temperature-depth (CTD) hydrography data
776	including pressure, temperature, total dissolved oxygen, conductivity, fluorescence, and beam
777	$transmission \ (\underline{https://doi.org/10.1575/1912/bco-dmo.783911.1}) \ and \ total \ dissolved \ metal, \ Zn \ and \ dissolved \ and \ dissolved \ dissolved \ and \ and \ and \ dissolved \ and \ $
778	Cd uptake rate, macronutrient, and pigment datasets are available through the NSF Biological
779	and Chemical Oceanography Data Management Office (BCO-DMO) repository
780	(https://doi.org/10.7284/907753). Underway pCO2 data collected during cruise NBP1801 are
781	available through R2R at https://doi.org/10.7284/139318 . The mass spectrometry global
782	proteomics data for CICLOPS bottle incubations and water column analyses have been deposited
783	with the ProteomeXchange Consortium through the PRIDE repository under the project name
784	"Zinc-iron co-limitation of natural marine phytoplankton assemblages in coastal Antarctica" with
785	project accession number PXD037056
786	$(https://www.ebi.ac.uk/pride/archive/projects/PXD037056).\ This \ data \ is \ accessible \ for \ review \ by$
787	using the following login information: username reviewer_pxd037056@ebi.ac.uk, password:
788	lFdOUoEb. The translated transcriptome used for spectrum to peptide matching has been
789	deposited in the National Center for Biotechnology Information sequence read archive under
790	BioProject accession no. PRJNA890306
791	(https://www.ncbi.nlm.nih.gov/bioproject/?term=PRJNA890306) and RNA-Seq BioSample
792	accession nos. SAMN31286421-SAMN31286522
793	(https://www.ncbi.nlm.nih.gov/biosample/?term=SAMN31286421).
794	
795	Acknowledgements
796	We thank the captain, crew, marine technicians and science party of RVIB Nathaniel B.

Palmer for their support and contributions to the success of the NBP18-01 cruise. We thank

Natalie Cohen for assistance and training with the SeaFAST. We thank Veronique Oldham for assistance with trace metal sampling. This work was funded by the National Science Foundation (2125063, 1643684, 1924554) and the Simons Foundation to M.A.S.; NSF-PLR 1643845 to R.B.D, NSF-CO (2123055) to M.A.S. and A.V.S., and the National Institutes of Health (GM135709-01A1 to M.A.S). Author contributions statement All authors contributed to data acquisition and analysis. RMK, NLS, LEL, RJC, DR, DMM, MRM, FB, RBD, GRD and MAS implemented the shipboard incubation study. RMK, MMB, RJC, DR, TJH, and AVS contributed to the formal analysis. NLS, LEL, FB, OM, RF, and GRD contributed to pigment datasets and interpretations. CB provided bacterial abundance data. RBD contributed DIC and in situ pCO2 data. AVS contributed analyses and discussion regarding historical pCO2 data and Zn-C growth limitation estimates. AEA contributed the metatranscriptome reference database used for proteomic analyses. RMK and MAS wrote the original draft. RMK, MAS, GRD, AVS, TJH, and RBD contributed to review and editing. All authors approved the final submitted manuscript. **Competing interests statement** The authors declare no competing interests.

798

799

800

801

802

803

804

805

806

807

808

809

810

811

812

813

814

815

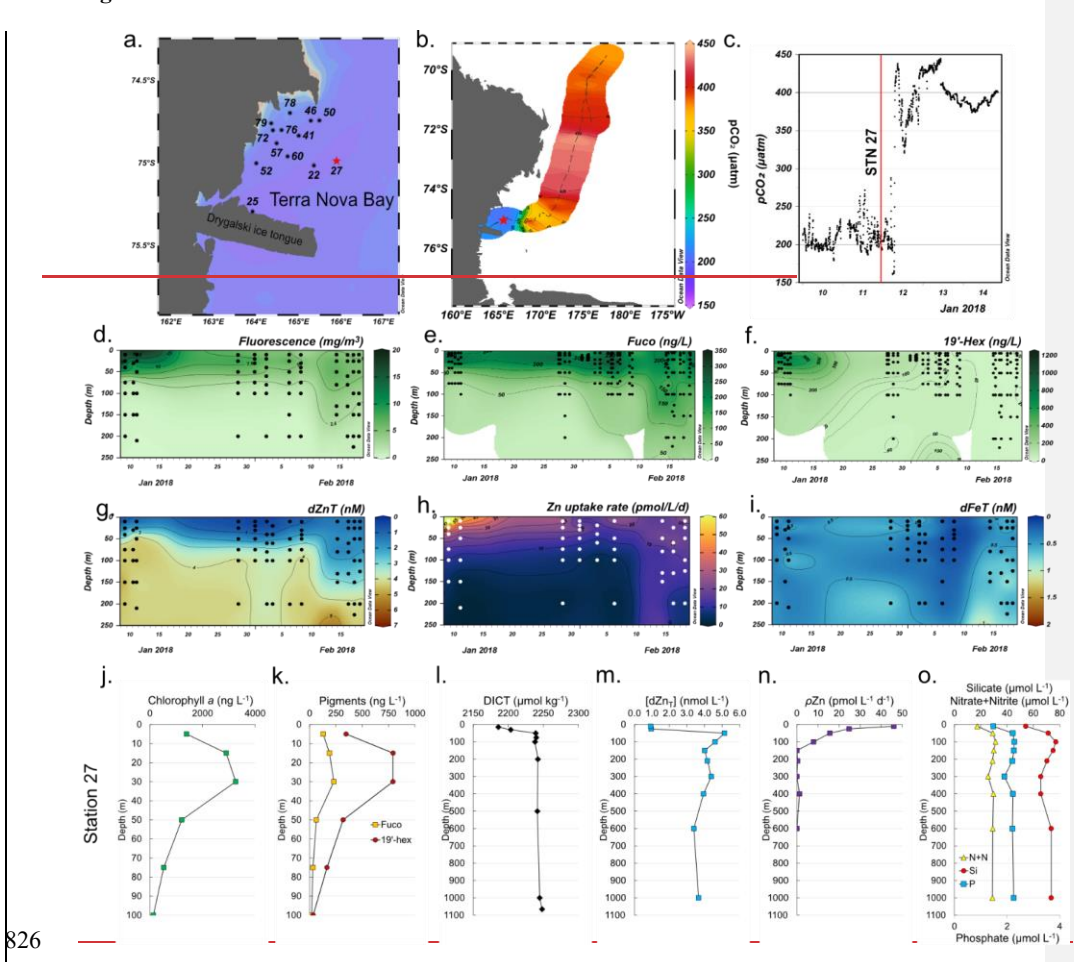
816

817

818

819

825 Figures



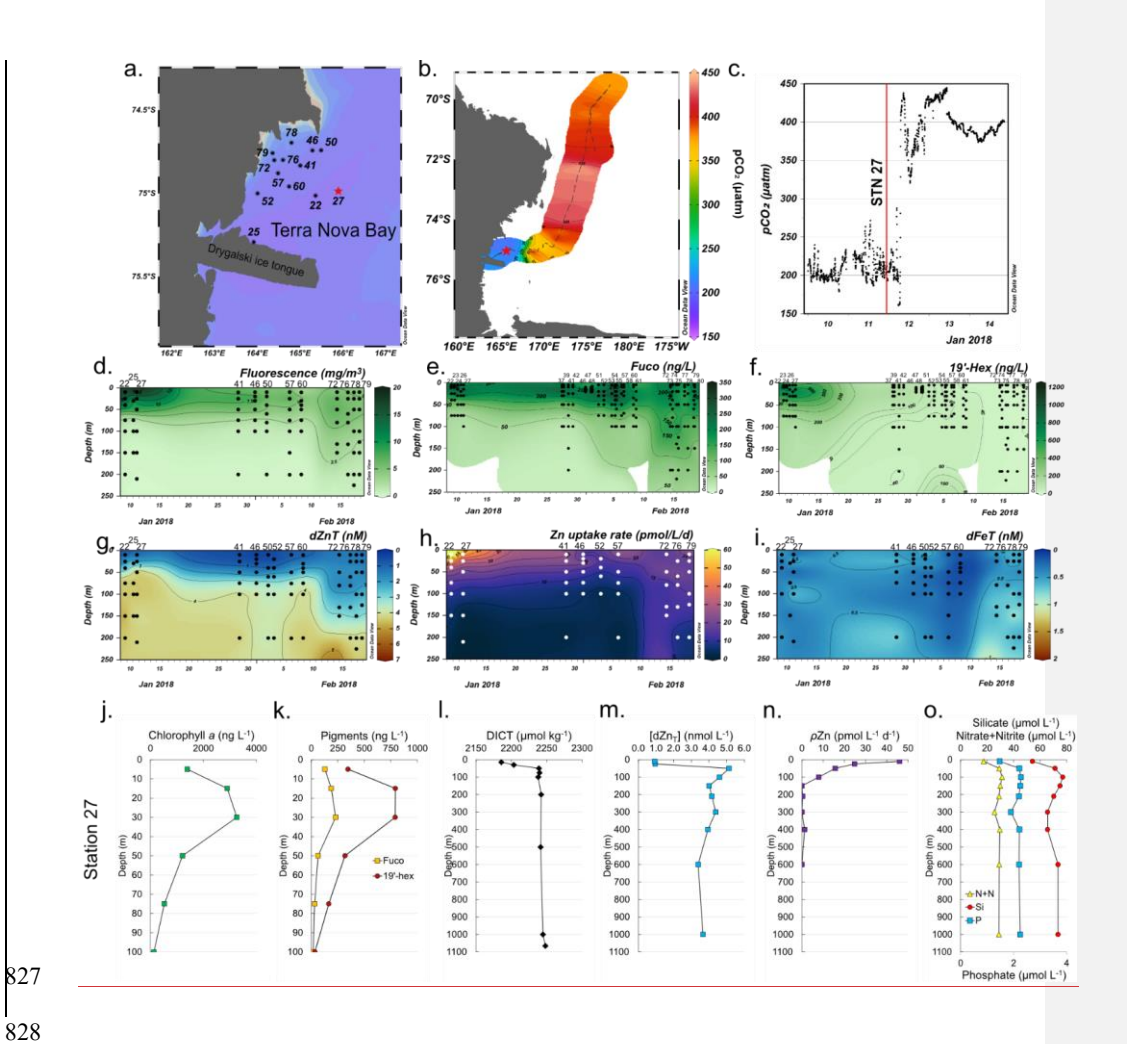


Figure 1. Temporal biogeochemistry of Terra Nova Bay and characterization of the experimental site at Station 27. (a) Sampling locations over the Ross Sea shelf in Terra Nova Bay, Antarctica. (b) Location of station 27 (red star) and surrounding seawater pCO₂ measured over a three-day transit northwards represented in color scale. (c) pCO₂ measured over time within TNB during the three-day transit shown in (b). The vertical red line denotes the pCO₂

level at the time of initial seawater collection at station 27. (d) Total chlorophyll fluorescence, (e) fucoxanthin (fuco), (f) 19' hexanoyloxyfucoxanthin (19'-hex), (g) total dissolved Zn, (h) total Zn uptake rates, and (i) total dissolved Fe measured in the upper 250 m represented on a color scale. Station data is presented in order of sampling date, from the earliest (Stn 22, early January) to the latest (Stn 79, late February). The data gap between January 13-23 occurred when the ship was unable to sample due to icebreaking duties for the McMurdo Station resupply ship. Stations indicated in (a) are those where the trace metal rosette (TMR) was deployed; pigment data was supplemented with additional TNB stations using a CTD (Table S2). Depth profiles of (j) chlorophyll a, (k) the pigments fuco and 19'hex, (l) total dissolved inorganic carbon (DICT), (m) total dissolved Zn, (n) total Zn uptake rates, and (o) the macronutrients nitrate+nitrite (N+N), phosphate (P), and silicate (Si) at the study site. Panels (d),(g),(h) and (i) were originally presented in Kell et al. (2024) and are reprised here to introduce the environmental context of the study site.

Formatted: Font: Italic

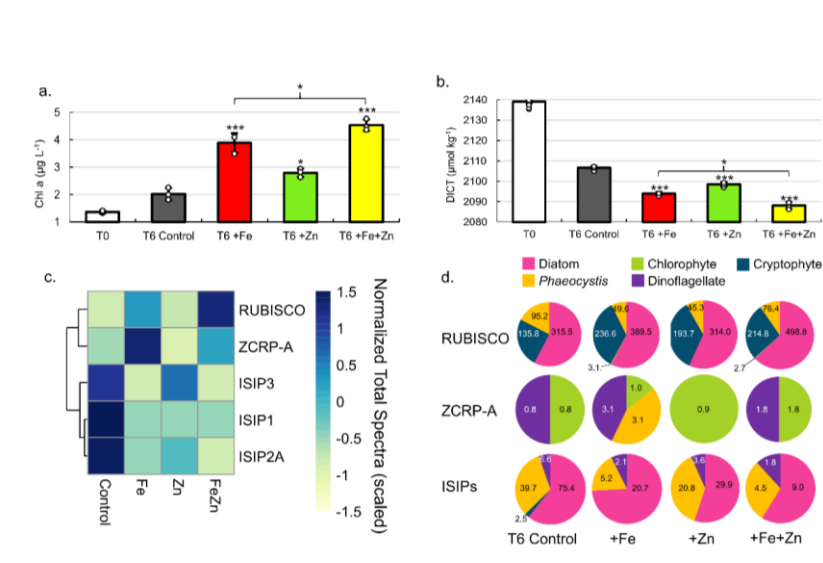


Figure 2. Evidence for Zn co-limitation with Fe in bottle incubations. (a) Chlorophyll a and (b) total DIC (DICT) at T0 (day 0) and in each treatment at T6 (day 6). Significant differences among groups were found using one-way ANOVA and post-hoc Dunnett test (*** p < 0.001, ** p < 0.01, * p < 0.05). Error bars are the standard deviation of biological triplicates (n=3). Individual data points are overlaid (white circles). (c) Heatmap of row-scaled exclusive protein spectral counts (normalized total spectra) showing relative protein abundance in each treatment. The dendrogram shows similarity in spectral abundance among samples based on Euclidean distance and hierarchical clustering. Color gradients represent low (yellow) to high (blue) protein expression. Ribulose-1,5-biphosphate carboxylase/oxygenase (RUBISCO), zinc/cobalt responsive protein A (ZCRP-A), and iron starvation induced proteins (ISIP1, ISIP2A, ISIP3) are shown. (d) Taxonomies assigned to RUBISCO, ZCRP-A, and ISIP proteins in each treatment at T6. Counts (normalized total spectra) assigned to each taxa are shown. ISIPs are the combined spectral counts of ISIP1A, ISIP2A and ISIP3.

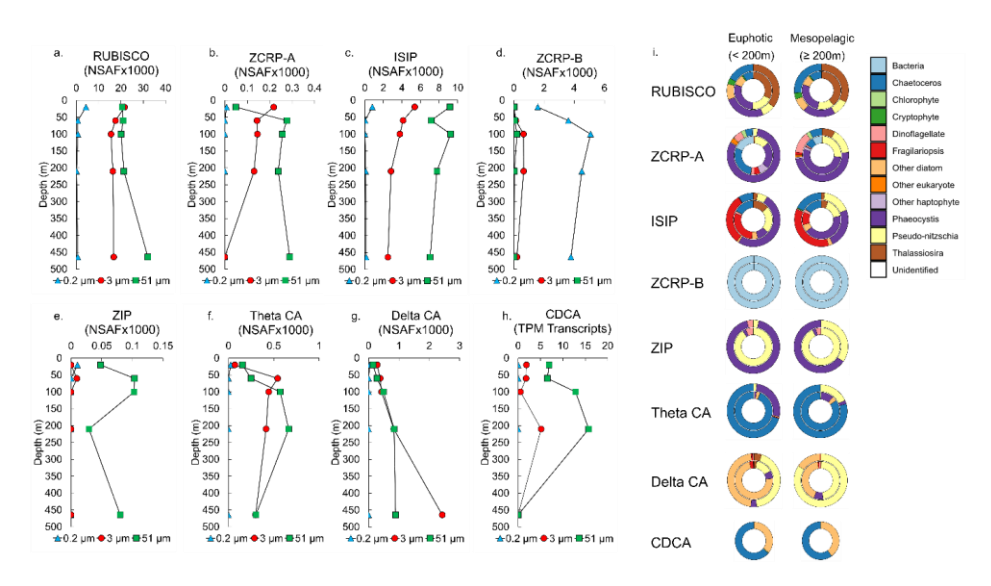


Figure 3. Metatranscriptomic and metaproteomic detection of Zn- and Fe-related proteins of interest at the experimental site. Depth profiles of summed NSAF-normalized protein spectral counts of (a) RUBISCO, (b) ZCRP-A, (c) iron starvation induced proteins (ISIPs), (d) ZCRP-B, (e) ZIP, (f) Theta CA, and (g) Delta CA detected from proteomic analysis of each filter size fraction (0.2, 3 and 51μm). (h) TPM-normalized transcript read counts of CDCA. (i) Stacked pie charts depicting relative community composition for proteins of interest for euphotic (< 200 m) and mesopelagic (≥ 200 m) depths. The outer rings show community composition based on NSAF-normalized protein spectral counts while the inner rings are TPM-normalized transcript read counts. Protein and transcript counts plotted in (i) were summed across all size fractions. ISIPs are the combined spectral counts of ISIP1A, ISIP2A and ISIP3.

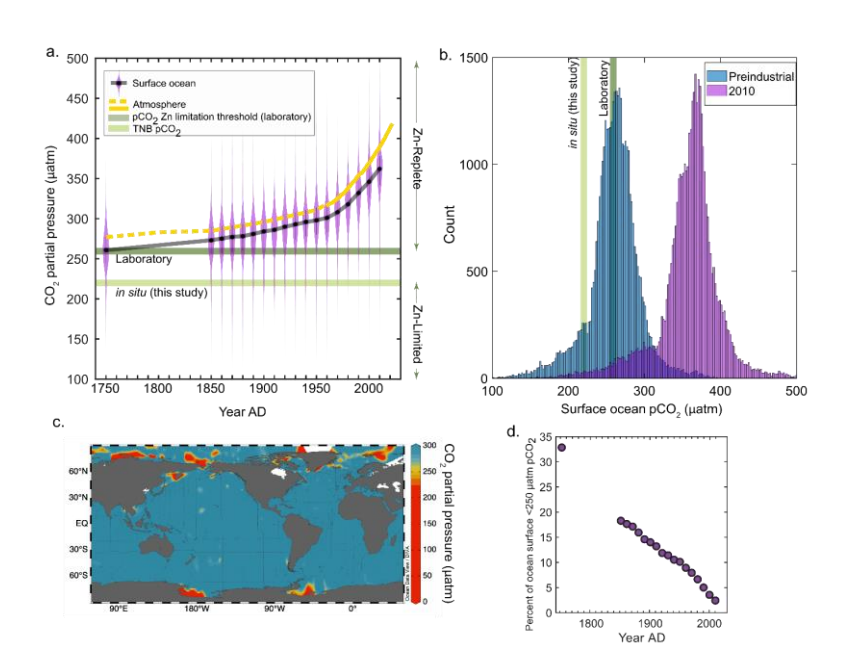


Figure 4. The partial pressure of CO₂ (pCO₂) and associated phytoplankton responses from this study and the literature. (a) Pre-industrial and decadal surface ocean pCO₂ reconstructions plotted as violin plots, with a running black line through the median values. The atmospheric curve is a composite of ice core data (dashed yellow line (Etheridge et al. 1996)) and the Mauna Loa record (solid yellow line (Keeling et al. 1976)). An estimated thresholds for zinc-limited

916	growth is plotted as the median of previous laboratory results (259 µatm, dark green line; see
917	Methods), and is compared to the <i>in situ</i> results of this study (220 μatm, light green line). (b)
918	Data in (a) plotted as a histogram comparing preindustrial and modern (2010) pCO2 values, with
919	the same pCO2 levels indicated. (c) Global map of surface ocean pCO2 plotted using
920	GLODAPv2.2022 data (Lauvset et al. 2022). (b) Percentage of the ocean surface less than 250
921	μatm pCO ₂ as a function of time. Surface ocean pCO ₂ reconstructions taken from Jiang et al.
922	2023.
923	
924	
925	
926	
927	
928	
929	References
930	Allen, A. E. and others. 2008. Whole-cell response of the pennate diatom Phaeodactylum
931	tricornutum to iron starvation. Proc. Natl. Acad. Sci. 105: 10438–10443.
932	doi:10.1073/pnas.0711370105
933	Altschul, S. F., W. Gish, W. Miller, E. W. Myers, and D. J. Lipman. 1990. Basic local alignment
934	search tool. J. Mol. Biol. doi:10.1016/S0022-2836(05)80360-2
935	Aramaki, T., R. Blanc-Mathieu, H. Endo, K. Ohkubo, M. Kanehisa, S. Goto, and H. Ogata.
936	2020. KofamKOALA: KEGG Ortholog assignment based on profile HMM and adaptive
937	score threshold A. Valencia [ed.]. Bioinformatics 36: 2251–2252.
938	doi:10.1093/bioinformatics/btz859

939	Arrigo, K. R., K. E. Lowry, and G. L. van Dijken. 2012. Annual changes in sea ice and
940	phytoplankton in polynyas of the Amundsen Sea, Antarctica. Deep Sea Res. Part II Top.
941	Stud. Oceanogr. 71–76 : 5–15. doi:10.1016/j.dsr2.2012.03.006
942	Baars, O., and P. L. Croot. 2011. The speciation of dissolved zinc in the Atlantic sector of the
943	Southern Ocean. Deep Sea Res. Part II Top. Stud. Oceanogr. 58: 2720–2732.
944	doi:10.1016/j.dsr2.2011.02.003
945	Balestra, C., L. Alonso-Sáez, J. M. Gasol, and R. Casotti. 2011. Group-specific effects on coastal
946	bacterioplankton of polyunsaturated aldehydes produced by diatoms. Aquat. Microb.
947	Ecol. doi:10.3354/ame01486
948	Behnke, J., and J. LaRoche. 2020. Iron uptake proteins in algae and the role of Iron Starvation-
949	Induced Proteins (ISIPs). Eur. J. Phycol. 55: 339–360.
950	doi:10.1080/09670262.2020.1744039
951	Bender, S. J. and others. 2018. Colony formation in Phaeocystis antarctica: connecting molecular
952	mechanisms with iron biogeochemistry. Biogeosciences 15: 4923-4942. doi:10.5194/bg-
953	15-4923-2018
954	Blaby-Haas, C. E., and S. S. Merchant. 2012. The ins and outs of algal metal transport. Biochim.
955	Biophys. Acta - Mol. Cell Res. 1823: 1531–1552. doi:10.1016/j.bbamcr.2012.04.010
956	Bolger, A. M., M. Lohse, and B. Usadel. 2014. Trimmomatic: a flexible trimmer for Illumina
957	sequence data. Bioinformatics 30: 2114–2120. doi:10.1093/bioinformatics/btu170
958	Browning, T. J., and C. M. Moore. 2023. Global analysis of ocean phytoplankton nutrient
959	limitation reveals high prevalence of co-limitation. Nat. Commun. 14: 5014.
960	doi:10.1038/s41467-023-40774-0

961	Bruland, K. W. 1980. Oceanographic distributions of cadmium, zinc, nickel, and copper in the
962	North Pacific. Earth Planet. Sci. Lett. 47: 176–198. doi:10.1016/0012-821X(80)90035-7
963	Bruland, K. W. 1989. Complexation of zinc by natural organic ligands in the central North
964	Pacific. Limnol. Oceanogr. 34: 269–285. doi:10.4319/lo.1989.34.2.0269
965	Buitenhuis, E. T., K. R. Timmermans, and H. J. W. de Baar. 2003. Zinc-bicarbonate colimitation
966	of Emiliania huxleyi. Limnol. Oceanogr. 48: 1575–1582. doi:10.4319/lo.2003.48.4.1575
967	Chavez, F. P., J. Sevadjian, C. Wahl, J. Friederich, and G. E. Friederich. 2018. Measurements of
968	pCO2 and pH from an autonomous surface vehicle in a coastal upwelling system. Deep
969	Sea Res. Part II Top. Stud. Oceanogr. 151: 137–146. doi:10.1016/j.dsr2.2017.01.001
970	Coale, K. H., R. Michael Gordon, and X. Wang. 2005. The distribution and behavior of
971	dissolved and particulate iron and zinc in the Ross Sea and Antarctic circumpolar current
972	along 170°W. Deep Sea Res. Part Oceanogr. Res. Pap. 52 : 295–318.
973	doi:10.1016/j.dsr.2004.09.008
974	Coale, K. H., X. Wang, S. J. Tanner, and K. S. Johnson. 2003. Phytoplankton growth and
975	biological response to iron and zinc addition in the Ross Sea and Antarctic Circumpolar
976	Current along 170°W. Deep Sea Res. Part II Top. Stud. Oceanogr. 50: 635–653.
977	doi:10.1016/S0967-0645(02)00588-X
978	Cochlan, W. P., D. A. Bronk, and K. H. Coale. 2002. Trace metals and nitrogenous nutrition of
979	Antarctic phytoplankton: experimental observations in the Ross Sea. Deep Sea Res. Part
980	II Top. Stud. Oceanogr. 49: 3365-3390. doi:10.1016/S0967-0645(02)00088-7
981	Cox, A. D., A. E. Noble, and M. A. Saito. 2014. Cadmium enriched stable isotope uptake and
982	addition experiments with natural phytoplankton assemblages in the Costa Rica
983	Upwelling Dome. Mar. Chem. 166: 70-81. doi:10.1016/j.marchem.2014.09.009

984	Crameri, F. 2023. Scientific colour maps.doi:10.5281/ZENODO.1243862
985	Crawford, D. W. and others. 2003a. Influence of zinc and iron enrichments on phytoplankton
986	growth in the northeastern subarctic Pacific Limitation of biomass and primary
987	production of phyto-plankton by dissolved iron (Fe) in high-nutrient, low-chlo.
988	Crawford, D. W. and others. 2003b. Influence of zinc and iron enrichments on phytoplankton
989	growth in the northeastern subarctic Pacific. Limnol. Oceanogr. 48: 1583-1600.
990	doi:10.4319/lo.2003.48.4.1583
991	Cullen, J. T., T. W. Lane, F. M. M. Morel, and R. M. Sheerell. 1999. Modulation of cadmium
992	uptake in phytoplankton by seawater CO2 concentration. Nature. doi:10.1038/46007
993	Cullen, J. T., and R. M. Sherrell. 2005. Effects of dissolved carbon dioxide, zinc, and manganese
994	on the cadmium to phosphorus ratio in natural phytoplankton assemblages. Limnol.
995	Oceanogr. 50: 1193–1204. doi:10.4319/lo.2005.50.4.1193
996	Cutter, G. A., and K. W. Bruland. 2012. Rapid and noncontaminating sampling system for trace
997	elements in global ocean surveys. Limnol. Oceanogr. Methods.
998	doi:10.4319/lom.2012.10.425
999	Dai, M. and others. 2022. Carbon Fluxes in the Coastal Ocean: Synthesis, Boundary Processes,
000	and Future Trends. Annu. Rev. Earth Planet. Sci. 50: 593-626. doi:10.1146/annurev-
001	earth-032320-090746
002	DeJong, H. B., R. B. Dunbar, D. Mucciarone, and D. A. Koweek. 2015. Carbonate saturation
003	state of surface waters in the Ross Sea and Southern Ocean: controls and implications for
004	the onset of aragonite undersaturation. Biogeosciences 12: 6881–6896. doi:10.5194/bg-
005	12-6881-2015

1006	Dickson, A. G., C. L. Sabine, and J. R. Christian, 2007. Guide to best practices for ocean CO2
1007	measurement. North Pacific Marine Science Organization.
1008	DiTullio, G. R. and others. 2000. Rapid and early export of Phaeocystis antarctica blooms in the
1009	Ross Sea, Antarctica. Nature. doi:10.1038/35007061
1010	DiTullio, G. R., N. Garcia, S. F. Riseman, and P. N. Sedwick. 2007. Effects of iron concentration
1011	on pigment composition in Phaeocystis antarctica grown at low irradiance.
1012	Biogeochemistry 83: 71-81. doi:10.1007/s10533-007-9080-8
1013	DiTullio, G. R., M. E. Geesey, A. Leventer, and M. P. Lizotte. 2003. Algal pigment ratios in the
1014	Ross Sea: Implications for Chemtax analysis of Southern Ocean data, p. 35–51. In.
1015	DiTullio, G. R., and W. O. Smith. 1996. Spatial patterns in phytoplankton biomass and pigment
1016	distributions in the Ross Sea. J. Geophys. Res. Oceans 101: 18467-18477.
1017	doi:10.1029/96JC00034
1018	Dreux Chappell, P., J. Vedmati, K. E. Selph, H. A. Cyr, B. D. Jenkins, M. R. Landry, and J. W.
1019	Moffett. 2016. Preferential depletion of zinc within Costa Rica upwelling dome creates
1020	conditions for zinc co-limitation of primary production. J. Plankton Res. 38: 244–255.
1021	doi:10.1093/plankt/fbw018
1022	Eddy, S. R. 2011. Accelerated Profile HMM Searches W.R. Pearson [ed.]. PLoS Comput. Biol.
1023	7: e1002195. doi:10.1371/journal.pcbi.1002195
1024	Edmonds, K. A., M. R. Jordan, and D. P. Giedroc. 2021. COG0523 proteins: a functionally
1025	diverse family of transition metal-regulated G3E P-loop GTP hydrolases from bacteria to
1026	man. Metallomics 13. doi:10.1093/mtomcs/mfab046
1027	Ellwood, M. J. 2004. Zinc and cadmium speciation in subantarctic waters east of New Zealand.
1028	Mar. Chem. doi:10.1016/j.marchem.2004.01.005

1029	Emms, D. M., and S. Kelly. 2022. SHOOT: phylogenetic gene search and ortholog inference.
1030	Genome Biol. 23. doi:10.1186/s13059-022-02652-8
1031	Etheridge, D. M., L. P. Steele, R. L. Langenfelds, R. J. Francey, JM. Barnola, and V. I.
1032	Morgan. 1996. Natural and anthropogenic changes in atmospheric CO 2 over the last
1033	1000 years from air in Antarctic ice and firn. J. Geophys. Res. Atmospheres 101: 4115-
1034	4128. doi:10.1029/95JD03410
1035	Fitzwater, S. E., K. S. Johnson, R. M. Gordon, K. H. Coale, and W. O. Smith. 2000. Trace metal
1036	concentrations in the Ross Sea and their relationship with nutrients and phytoplankton
1037	growth. Deep-Sea Res. Part II Top. Stud. Oceanogr. 47: 3159-3179. doi:10.1016/S0967-
1038	0645(00)00063-1
1039	Fourquez, M., M. Bressac, S. L. Deppeler, M. Ellwood, I. Obernosterer, T. W. Trull, and P. W.
1040	Boyd. 2020. Microbial Competition in the Subpolar Southern Ocean: An Fe-C Co-
1041	limitation Experiment. Front. Mar. Sci. 6: 776. doi:10.3389/fmars.2019.00776
1042	Franck, V., K. Bruland, D. Hutchins, and M. Brzezinski. 2003. Iron and zinc effects on silicic
1043	acid and nitrate uptake kinetics in three high-nutrient, low-chlorophyll (HNLC) regions.
1044	Mar. Ecol. Prog. Ser. 252: 15–33. doi:10.3354/meps252015
1045	Fukuda, R., Y. Sohrin, N. Saotome, H. Fukuda, T. Nagata, and I. Koike. 2000. East—west
1046	gradient in ectoenzyme activities in the subarctic Pacific: Possible regulation by zinc.
1047	Limnol. Oceanogr. 45: 930-939. doi:10.4319/lo.2000.45.4.0930
1048	Harrison, C. S., M. C. Long, N. S. Lovenduski, and J. K. Moore. 2018. Mesoscale Effects on
1049	Carbon Export: A Global Perspective. Glob. Biogeochem. Cycles 32: 680-703.
1050	doi:10.1002/2017GB005751

1051	Jakuba, R. W., M. A. Saito, J. W. Moffett, and Y. Xu. 2012. Dissolved zinc in the subarctic
1052	North Pacific and Bering Sea: Its distribution, speciation, and importance to primary
1053	producers. Glob. Biogeochem. Cycles. doi:10.1029/2010GB004004
1054	Jensen, E. L., S. C. Maberly, and B. Gontero. 2020a. Insights on the Functions and
1055	Ecophysiological Relevance of the Diverse Carbonic Anhydrases in Microalgae. Int. J.
1056	Mol. Sci. 21: 2922. doi:10.3390/ijms21082922
1057	Jensen, L. T., N. J. Wyatt, W. M. Landing, and J. N. Fitzsimmons. 2020b. Assessment of the
1058	stability, sorption, and exchangeability of marine dissolved and colloidal metals. Mar.
1059	Chem. 220: 103754. doi:10.1016/j.marchem.2020.103754
1060	Jiang, L. and others. 2023. Global Surface Ocean Acidification Indicators From 1750 to 2100. J.
1061	Adv. Model. Earth Syst. 15: e2022MS003563. doi:10.1029/2022MS003563
1062	Keeling, C. D., R. B. Bacastow, A. E. Bainbridge, C. A. Ekdahl, P. R. Guenther, L. S.
1063	Waterman, and J. F. S. Chin. 1976. Atmospheric carbon dioxide variations at Mauna Loa
1064	Observatory, Hawaii. Tellus Dyn. Meteorol. Oceanogr. 28: 538.
1065	doi:10.3402/tellusa.v28i6.11322
1066	Kell, R. M. and others. 2024. High metabolic zinc demand within native Amundsen and Ross sea
1067	phytoplankton communities determined by stable isotope uptake rate measurements.
1068	Biogeosciences 21: 5685-5706. doi:10.5194/bg-21-5685-2024
1069	Kellogg, R. M. and others. 2022a. Adaptive responses of marine diatoms to zinc scarcity and
1070	ecological implications. Nat. Commun. 2022 131 13: 1-13. doi:10.1038/s41467-022-
1071	29603-у
1072	Kellogg, R. M., M. R. McIlvin, J. Vedamati, B. S. Twining, J. W. Moffett, A. Marchetti, D. M.
1073	Moran, and M. A. Saito. 2020. Efficient zinc/cobalt inter-replacement in northeast Pacific

1074	diatoms and relationship to high surface dissolved Co: Zn ratios. Limnol. Oceanogr. 65:
1075	2557–2582. doi:10.1002/lno.11471
1076	Kellogg, R. M., D. M. Moran, M. R. McIlvin, A. V. Subhas, A. E. Allen, and M. A. Saito.
1077	2022b. Lack of a Zn/Co substitution ability in the polar diatom Chaetoceros neogracile
1078	RS19. Limnol. Oceanogr. 67: 2265–2280. doi:10.1002/lno.12201
1079	Krogh, A., B. Larsson, G. von Heijne, and E. L. L. Sonnhammer. 2001. Predicting
1080	transmembrane protein topology with a hidden markov model: application to complete
1081	genomes11Edited by F. Cohen. J. Mol. Biol. 305: 567-580. doi:10.1006/jmbi.2000.4315
1082	Krumhardt, K. M., N. S. Lovenduski, M. D. Iglesias-Rodriguez, and J. A. Kleypas. 2017.
1083	Coccolithophore growth and calcification in a changing ocean. Prog. Oceanogr. 159:
1084	276–295. doi:10.1016/j.pocean.2017.10.007
1085	Lampe, R. H. and others. 2018. Different iron storage strategies among bloom-forming diatoms.
1086	Proc. Natl. Acad. Sci. 115. doi:10.1073/pnas.1805243115
1087	Lane, T. W., and F. M. Morel. 2000a. A biological function for cadmium in marine diatoms.
1088	Proc. Natl. Acad. Sci. U. S. A. 97: 4627–31. doi:10.1073/pnas.090091397
1089	Lane, T. W., and F. M. M. Morel. 2000b. Regulation of Carbonic Anhydrase Expression by
1090	Zinc, Cobalt, and Carbon Dioxide in the Marine Diatom Thalassiosira weissflogii. Plant
1091	Physiol. 123: 345–352. doi:10.1104/pp.123.1.345
1092	Lauvset, S. K. and others. 2022. GLODAPv2.2022: the latest version of the global interior ocean
1093	biogeochemical data product. Earth Syst. Sci. Data 14: 5543-5572. doi:10.5194/essd-14-
1094	5543-2022

1095	Lhospice, S. and others. 2017. Pseudomonas aeruginosa zinc uptake in chelating environment is
1096	primarily mediated by the metallophore pseudopaline. Sci. Rep. 7: 17132.
1097	doi:10.1038/s41598-017-16765-9
1098	Li, B., and C. N. Dewey. 2011. RSEM: accurate transcript quantification from RNA-Seq data
1099	with or without a reference genome. BMC Bioinformatics 12: 323. doi:10.1186/1471-
1100	2105-12-323
1101	Lohan, M. C., P. J. Statham, and D. W. Crawford. 2002. Total dissolved zinc in the upper water
1102	column of the subarctic North East Pacific. Deep Sea Res. Part II Top. Stud. Oceanogr.
1103	49 : 5793–5808. doi:10.1016/S0967-0645(02)00215-1
1104	Lu, X., and H. Zhu. 2005. Tube-Gel Digestion. Mol. Cell. Proteomics 4: 1948–1958.
1105	doi:10.1074/mcp.m500138-mcp200
1106	Mangoni, O., M. Saggiomo, F. Bolinesi, M. Castellano, P. Povero, V. Saggiomo, and G. R.
1107	DiTullio. 2019. Phaeocystis antarctica unusual summer bloom in stratified antarctic
1108	coastal waters (Terra Nova Bay, Ross Sea). Mar. Environ. Res.
1109	doi:10.1016/j.marenvres.2019.05.012
1110	Martin, J. H., S. E. Fitzwater, and R. M. Gordon. 1990. Iron deficiency limits phytoplankton
1111	growth in Antarctic waters. Glob. Biogeochem. Cycles 4: 5-12.
1112	doi:10.1029/GB004i001p00005
1113	Mazzotta, M. G., M. R. McIlvin, D. M. Moran, D. T. Wang, K. D. Bidle, C. H. Lamborg, and M.
1114	A. Saito. 2021. Characterization of the metalloproteome of Pseudoalteromonas (BB2-
1115	AT2): biogeochemical underpinnings for zinc, manganese, cobalt, and nickel cycling in a
1116	ubiquitous marine heterotroph. Metallomics 13. doi:10.1093/mtomcs/mfab060

1117	McIlvin, M. R., and M. A. Saito. 2021. Online Nanoflow Two-Dimension Comprehensive
1118	Active Modulation Reversed Phase-Reversed Phase Liquid Chromatography High-
1119	Resolution Mass Spectrometry for Metaproteomics of Environmental and Microbiome
1120	Samples. J. Proteome Res. 20: 4589–4597. doi:10.1021/acs.jproteome.1c00588
1121	Middag, R., H. J. W. De Baar, and K. W. Bruland. 2019. The Relationships Between Dissolved
1122	Zinc and Major Nutrients Phosphate and Silicate Along the GEOTRACES GA02
1123	Transect in the West Atlantic Ocean. Glob. Biogeochem. Cycles 33: 63-84.
1124	doi:10.1029/2018GB006034
1125	Milner, M. J., J. Seamon, E. Craft, and L. V. Kochian. 2013. Transport properties of members of
1126	the ZIP family in plants and their role in Zn and Mn homeostasis. J. Exp. Bot. 64: 369-
1127	381. doi:10.1093/jxb/ers315
1128	Moore, C. M. and others. 2013. Processes and patterns of oceanic nutrient limitation. Nat.
1129	Geosci. 6: 701–710. doi:10.1038/ngeo1765
1130	Morel, F. M. M., J. R. Reinfelder, S. B. Roberts, C. P. Chamberlain, J. G. Lee, and D. Yee. 1994.
1131	Zinc and carbon co-limitation of marine phytoplankton. Nature 369: 740-742.
1132	doi:10.1038/369740A0
1133	Mortazavi, A., B. A. Williams, K. McCue, L. Schaeffer, and B. Wold. 2008. Mapping and
1134	quantifying mammalian transcriptomes by RNA-Seq. Nat. Methods 5: 621-628.
1135	doi:10.1038/nmeth.1226
1136	Obernosterer, I., M. Fourquez, and S. Blain. 2015. Fe and C co-limitation of heterotrophic
1137	bacteria in the naturally fertilized region off the Kerguelen Islands. Biogeosciences 12:
1138	1983–1992. doi:10.5194/bg-12-1983-2015

1139	Podell, S., and T. Gaasterland. 2007. DarkHorse: a method for genome-wide prediction of
1140	horizontal gene transfer. Genome Biol. 8: R16. doi:10.1186/gb-2007-8-2-r16
1141	Rapp, I., C. Schlosser, D. Rusiecka, M. Gledhill, and E. P. Achterberg. 2017. Automated
1142	preconcentration of Fe, Zn, Cu, Ni, Cd, Pb, Co, and Mn in seawater with analysis using
1143	high-resolution sector field inductively-coupled plasma mass spectrometry. Anal. Chim.
1144	Acta. doi:10.1016/j.aca.2017.05.008
1145	Redfield, A. C. 1958. The Biological Control of Chemical Factors in the Environment. Am. Sci.
1146	doi:10.2307/27828530
1147	Rho, M., H. Tang, and Y. Ye. 2010. FragGeneScan: predicting genes in short and error-prone
1148	reads. Nucleic Acids Res. 38: e191-e191. doi:10.1093/nar/gkq747
1149	Riebesell, U., D. A. Wolf-Gladrow, and V. Smetacek. 1993. Carbon dioxide limitation of marine
1150	phytoplankton growth rates. Nature 361: 249–251. doi:10.1038/361249a0
1151	Robbins, L. L. and others. 2018. Spatial and Temporal Variability of pCO_2 , Carbon Fluxes, and
1152	Saturation State on the West Florida Shelf. J. Geophys. Res. Oceans 123: 6174-6188.
1153	doi:10.1029/2018JC014195
1154	Roshan, S., T. DeVries, J. Wu, and G. Chen. 2018. The Internal Cycling of Zinc in the Ocean.
1155	Glob. Biogeochem. Cycles 32: 1833–1849. doi:10.1029/2018GB006045
1156	Saito, M. A., and T. J. Goepfert. 2008. Zinc-cobalt colimitation of <i>Phaeocystis antarctica</i> .
1157	Limnol. Oceanogr. 53: 266-275. doi:10.4319/lo.2008.53.1.0266
1158	Saito, M. A., T. J. Goepfert, and J. T. Ritt. 2008. Some thoughts on the concept of colimitation:
1159	Three definitions and the importance of bioavailability. Limnol. Oceanogr. 53 : 276–290.
1160	doi:10.4319/lo.2008.53.1.0276

1161	Schanke, N. L., F. Bolinesi, O. Mangoni, C. Katlein, P. Anhaus, M. Hoppmann, P. A. Lee, and
1162	G. R. DiTullio. 2021. Biogeochemical and ecological variability during the late summer-
1163	early autumn transition at an ice-floe drift station in the Central Arctic Ocean. Limnol.
1164	Oceanogr. doi:10.1002/lno.11676
1165	Scharek, R., M. A. Van Leeuwe, and H. J. W. De Baar. 1997. Responses of Southern Ocean
1166	phytoplankton to the addition of trace metals. Deep-Sea Res. Part II Top. Stud. Oceanogr.
1167	doi:10.1016/S0967-0645(96)00074-4
1168	Schmieder, R., Y. W. Lim, and R. Edwards. 2012. Identification and removal of ribosomal RNA
1169	sequences from metatranscriptomes. Bioinformatics 28: 433-435.
1170	doi:10.1093/bioinformatics/btr669
1171	Schneider, B., and J. D. Müller. 2018. Biogeochemical transformations in the Baltic Sea:
1172	observations through carbon dioxide glasses, Springer.
1173	Sharma, D., H. Biswas, S. Silori, D. Bandyopadhyay, A. urRahman Shaik, D. Cardinal, M.
1174	Mandeng-Yogo, and D. Ray. 2020. Impacts of Zn and Cu enrichment under ocean
1175	acidification scenario on a phytoplankton community from tropical upwelling system.
1176	Mar. Environ. Res. 155: 104880. doi:10.1016/j.marenvres.2020.104880
1177	Sharp, J. D., D. Pierrot, M. P. Humphreys, JM. Epitalon, J. C. Orr, E. R. Lewis, and D. W. R.
1178	Wallace. 2023. CO2SYSv3 for MATLAB.doi:10.5281/ZENODO.3950562
1179	Shim, J., D. Kim, Y. C. Kang, J. H. Lee, ST. Jang, and CH. Kim. 2007. Seasonal variations in
1180	pCO2 and its controlling factors in surface seawater of the northern East China Sea. Cont.
1181	Shelf Res. 27: 2623–2636. doi:10.1016/j.csr.2007.07.005
1182	Sieber, M., T. M. Conway, G. F. de Souza, C. S. Hassler, M. J. Ellwood, and D. Vance. 2020.
1183	Cycling of zinc and its isotopes across multiple zones of the Southern Ocean: Insights

1184	from the Antarctic Circumnavigation Expedition. Geochim. Cosmochim. Acta.
1185	doi:10.1016/j.gca.2019.09.039
1186	Smith, W. O., A. R. Shields, J. A. Peloquin, G. Catalano, S. Tozzi, M. S. Dinniman, and V. A.
1187	Asper. 2006. Interannual variations in nutrients, net community production, and
1188	biogeochemical cycles in the Ross Sea. Deep-Sea Res. Part II Top. Stud. Oceanogr.
1189	doi:10.1016/j.dsr2.2006.02.014
1190	Sperfeld, E., D. Raubenheimer, and A. Wacker. 2016. Bridging factorial and gradient concepts
1191	of resource co-limitation: towards a general framework applied to consumers J. Grover
1192	[ed.]. Ecol. Lett. 19: 201–215. doi:10.1111/ele.12554
1193	Subhas, A. V., J. F. Adkins, S. Dong, N. E. Rollins, and W. M. Berelson. 2019. The carbonic
1194	anhydrase activity of sinking and suspended particles in the North Pacific Ocean. Limnol
1195	Oceanogr. 65: 637–651. doi:10.1002/lno.11332
1196	Sun, Y., P. Debeljak, and I. Obernosterer. 2021. Microbial iron and carbon metabolism as
1197	revealed by taxonomy-specific functional diversity in the Southern Ocean. ISME J. 15:
1198	2933–2946. doi:10.1038/s41396-021-00973-3
1199	Sunda, W. G., and S. A. Huntsman. 1995. Cobalt and zinc interreplacement in marine
1200	phytoplankton: Biological and geochemical implications. Limnol. Oceanogr. 40: 1404-
1201	1417. doi:10.4319/lo.1995.40.8.1404
1202	Sunda, W. G., and S. A. Huntsman. 2000. Effect of Zn, Mn, and Fe on Cd accumulation in
1203	phytoplankton: Implications for oceanic Cd cycling. Limnol. Oceanogr. 45: 1501-1516.
1204	doi:10.4319/lo.2000.45.7.1501

1205	Sunda, W. G., and S. A. Huntsman. 2005. Effect of CO 2 supply and demand on zinc uptake and
1206	growth limitation in a coastal diatom. Limnol. Oceanogr. 50: 1181-1192.
1207	doi:10.4319/lo.2005.50.4.1181
1208	Takahashi, T., S. C. Sutherland, and A. Kozyr. 2020. Global Ocean Surface Water Partial
1209	Pressure of CO2 Database (LDEO Database Version 2019): Measurements Performed
1210	During 1957-2019 (NCEI Accession 0160492). NOAA Natl. Cent. Environ. Inf.
1211	Tatusov, R. L. and others. 2003. The COG database: an updated version includes eukaryotes.
1212	BMC Bioinformatics 4: 41. doi:10.1186/1471-2105-4-41
1213	Tortell, P. D., M. C. Long, C. D. Payne, AC. Alderkamp, P. Dutrieux, and K. R. Arrigo. 2012.
1214	Spatial distribution of pCO2, Δ O2/Ar and dimethylsulfide (DMS) in polynya waters and
1215	the sea ice zone of the Amundsen Sea, Antarctica. Deep Sea Res. Part II Top. Stud.
1216	Oceanogr. 71–76: 77–93. doi:10.1016/j.dsr2.2012.03.010
1217	Tortell, P. D., C. Payne, C. Gueguen, R. F. Strzepek, P. W. Boyd, and B. Rost. 2008. Inorganic
1218	carbon uptake by Southern Ocean phytoplankton. Limnol. Oceanogr. 53: 1266–1278.
1219	doi:10.4319/lo.2008.53.4.1266
1220	Twining, B. S., and S. B. Baines. 2013. The trace metal composition of marine phytoplankton.
1221	Annu. Rev. Mar. Sci. 5: 191–215. doi:10.1146/annurev-marine-121211-172322
1222	Valerio, A. M., M. Kampel, N. D. Ward, H. O. Sawakuchi, A. C. Cunha, and J. E. Richey. 2021.
1223	CO2 partial pressure and fluxes in the Amazon River plume using in situ and remote
1224	sensing data. Cont. Shelf Res. 215: 104348. doi:10.1016/j.csr.2021.104348
1225	Wuttig, K. and others. 2019. Critical evaluation of a seaFAST system for the analysis of trace
1226	metals in marine samples. Talanta. doi:10.1016/j.talanta.2019.01.047

1227	Wyatt, N. J., A. Milne, E. M. S. Woodward, A. P. Rees, T. J. Browning, H. A. Bouman, P. J.
1228	Worsfold, and M. C. Lohan. 2014. Biogeochemical cycling of dissolved zinc along the
1229	GEOTRACES South Atlantic transect GA10 at 40°S. Glob. Biogeochem. Cycles 28: 44-
1230	56. doi:10.1002/2013GB004637
1231	Xu, Y., D. Shi, L. Aristilde, and F. M. M. Morel. 2012. The effect of pH on the uptake of zinc
1232	and cadmium in marine phytoplankton: Possible role of weak complexes. Limnol.
1233	Oceanogr. doi:10.4319/lo.2012.57.1.0293
1234	Ye, N. and others. 2022. The role of zinc in the adaptive evolution of polar phytoplankton. Nat.
1235	Ecol. Evol. 6 : 965–978. doi:10.1038/s41559-022-01750-x
1236	Zhang, Y., Z. Wen, M. P. Washburn, and L. Florens. 2010. Refinements to Label Free Proteome
1237	Quantitation: How to Deal with Peptides Shared by Multiple Proteins. Anal. Chem. 82:
1238	2272–2281. doi:10.1021/ac9023999
1239	
1240	Supplementary information for "Zinc stimulation of phytoplankton in a low carbon
1241	dioxide, coastal Antarctic environment: evidence for the Zn hypothesis"
1242	
1243	Supplementary Table 1. Summary of zinc incubation experiments in marine environments
1244	Note that all experiments focus on phytoplankton populations with the exception of Fukada et al
1245	(2000) and Mazzotta et al. (2021) which focus on bacterial heterotrophy. This list represents our
1246	knowledge of the literature but may be incomplete.
1247	

Study	Location	Zn Treatment Replication	pCO ₂	Dissolved Environmental Zn Data	Zn Response
Scharek et al. 1997(Scharek et al. 1997)	Southern Ocean	Zn n=2, control n=1	No	No	Negative/"very small"
Fukada et al., 2000(Fukuda et al. 2000)	North Pacific	Integrated water column leucine aminopeptidase activity (0- 100m)	No	Yes	Leucine aminopeptidase activity positively correlated with dZn
Cochlan et al. 2002(Cochlan et al. 2002)	Western Ross Sea	None (n=1 +Zn, +Zn+Fe)	No	No	Increase in specific uptake of NO ₃ -
Coale et al. 2003(Coale et al. 2003)	Ross Sea, Southern Ocean	None (n=1 +Zn, +Zn+Fe)	No	Yes	Negative/"very small"
Crawford et al. 2003(Crawford et al. 2003a)	Northeast Pacific Ocean	Triplicate (n=3)	Yes	No	"Slightly but significantly" altered Chl, nitrate and phosphate

Franck et al. 2003(Franck et al. 2003)	Costa Rica Dome	Triplicate (n=3)	No	No	Secondary Zn limitation after Fe in diatom microscopy data
Ellwood 2004(Ellwood 2004)	Subantarctic	Duplicates (n=2)	No	Yes	Negative
Cullen et al. 1999; Cullen and Sherrell 2005(Cullen et al. 1999; Cullen and Sherrell 2005)	Coastal California	Duplicates (n=2)	No	No	Enhanced Cd:P in low pCO ₂ treatments, decrease in Cd:P with Zn addition
Jakuba et al. 2012(Jakuba et al. 2012)	North Pacific	Singlicate with timepoints sacrificed	No	Yes	Primary, no additive effect with iron.
Dreux Chappell et al. 2016(Dreux Chappell et al. 2016)	Costa Rica Dome	Triplicate (n=3)	No	Yes	Secondary limitation with

Sharma et al. 2020(Sharma et al. 2020)	Eastern Arabian Sea	Triplicate (n=3)	Yes	No	Negative/ "insignificant effects"
Mazzotta et al. 2021(Mazzotta et al. 2021)	Equatorial Pacific	Quintuplicate (n=5) sediment trap incubations	No	Yes in separate study (Cohen et al., 2021)	Enhancement of alkaline phosphatase activity with Zn addition in sediment trap samples
This study	Terra Nova Bay, Ross Sea	Triplicate (n=3)	Yes	Yes	Primary and Secondary limitation. Independent validation by Zn biomarkers.

Supplementary Table 2. Station metadata for the NBP18-01 cruise. Stations at which total Zn uptake rates were determined are indicated by asterisks (*).

Station	Latitude (°N)	Longitude (°E)	Sampling Date
Station	Latitude (IV)	Longitude (L)	(yyyy-mm-dd hh:mm)
4*	-72.751	-116.001	2017-12-30 01:23

10	-73.054	-129.988	2018-01-03 03:39		
11*	-74.047	-133.764	2018-01-03 19:58		
15*	-75.864	-151.918	2018-01-05 14:51		
20*	-76.714	179.819	2018-01-08 02:00		
22*	-75.013	165.358	2018-01-09 15:56		
<u>23</u>	-75.003	165.781	2018-01-01 3:51	•	Formatted Tab
<u>24</u>	<u>-75.031</u>	165.551	2018-01-10 16:33		
25	-75.293	163.914	2018-01-11 01:26		
<u>26</u>	<u>-75.139</u>	<u>164.836</u>	2018-01-11 5:14	4	Formatted Tabl
27*	-74.987	165.890	2018-01-11 16:05		
29*	-76.001	172.997	2018-01-16 03:00		
31	-77.295	175.390	2018-01-17 04:39		
32*	-76.750	172.000	2018-01-17 19:19		
34	-77.147	168.503	2018-01-23 22:59		
35*	-76.231	168.769	2018-01-26 20:17		
<u>37</u>	<u>-75.001</u>	164.999	2018-01-27 23:21	•	Formatted Table
<u>39</u>	<u>-75.001</u>	<u>164.170</u>	2018-01-28 6:00		
41*	-74.833	165.002	2018-01-29 00:41		
<u>42</u>	<u>-75.166</u>	<u>164.169</u>	2018-01-29 19:30	4	Formatted Table
46*	-74.742	165.287	2018-01-31 21:32		
<u>47</u>	<u>-74.877</u>	164.249	2018-02-01 19:28	4	Formatted Table
<u>48</u>	<u>-74.873</u>	164.670	2018-02-01 23:30		
50	-74.741	165.488	2018-02-02 21:17		

<u>51</u>	<u>-75.000</u>	<u>164.498</u>	2018-02-03 0:46	Formatted Table
52*	-75.000	164.005	2018-02-03 21:43	
<u>53</u>	<u>-74.980</u>	164.441	2018-02-05 5:30	Formatted Table
<u>54</u>	<u>-74.750</u>	<u>164.169</u>	2018-02-05 19:26	
<u>55</u>	<u>-74.751</u>	165.498	2018-02-06 0:10	
57*	-74.879	164.482	2018-02-06 20:12	
<u>58</u>	<u>-74.893</u>	164.843	2018-02-07 5:26	Formatted Table
60	-74.959	164.739	2018-02-08 20:06	
<u>61</u>	<u>-74.807</u>	164.773	2018-02-09 6:35	Formatted Table
62*	-74.999	169.491	2018-02-09 19:27	
67*	-76.454	167.919	2018-02-11 19:19	
70	-74.744	170.374	2018-02-13 21:25	
72*	-74.800	164.395	2018-02-14 22:28	
<u>73</u>	<u>-75.037</u>	164.503	2018-02-15 7:03	Formatted Table
<u>74</u>	<u>-74.839</u>	164.531	2018-02-15 23:18	
<u>75</u>	<u>-74.790</u>	<u>164.677</u>	2018-02-16 6:22	
76*	-74.799	164.597	2018-02-16 20:15	
<u>77</u>	<u>-74.863</u>	165.764	2018-02-17 6:59	Formatted Table
78	-74.696	164.796	2018-02-17 20:34	
79*	-74.757	164.356	2018-02-18 19:29	Formatted Table
<u>80</u>	<u>-74.637</u>	<u>164.792</u>	2018-02-18 23:00	

Supplementary Table 3. Summary of ANOVA statistics for T6 incubation treatments comparing measured parameters. Significant differences among groups were found using one-way ANOVA and post-hoc Dunnett test (*** p < 0.001, ** p < 0.01, * p < 0.05, . p < 0.1). Chl a, chlorophyll a; DIC_T, total dissolved inorganic carbon; chl b, chlorophyll b; Prasino, prasinoxanthin; fuco, fucoxanthin; 19'hex, 19'-hexanoyloxyfucoxanthin; chl c3, chlorophyll c3. NA, no statistically significant difference. All parameters were measured in biological triplicate.

									Bacteri
Treatmen	Chl a	$\mathrm{DIC}_{\mathrm{T}}$	Chl b	Prasino	Fuco	19'hex	Fuco:he	Hex:Ch	al
t (T6)	Ciii u	Die	Cm v	Tushio	1 dec	17 Hex	X	1 c3	abunda
									nce
+Fe vs	<i>p</i> =	<i>p</i> =	<i>p</i> =	<i>p</i> =		p = 8e-	<i>p</i> =	<i>p</i> =	p =
	9.5e-5	5.3e-6	4.0e-3	2.9e-2	NA	3	4.2e-4	2.0e-4	9.1e-4
Ctrl	(***)	(***)	(**)	(*)		(**)	(***)	(***)	(***)
+Zn vs	<i>p</i> =	p =	<i>p</i> =	<i>p</i> =	NA	NA	NA	<i>p</i> =	NA
Ctrl	1.1e-2	5.0e-6	8.0e-2	7.4e-3	INA	INA	INA	0.02520	INA

	(*)	(***)	(.)	(**)				(*)	
+FeZn vs	<i>p</i> =	p =	p =	p =			<i>p</i> =	<i>p</i> =	<i>p</i> =
	1.3e-7	2.2e-16	4.0e-4	5.7e-2	NA	NA	2.7e-3	1.9e-4	6.3e-4
Ctrl	(***)	(***)	(***)	(.)			(**)	(***)	(***)
+FeZn vs	p =	p =				<i>p</i> =			
+Fe	3.4e-2	4.4e-3	NA	NA	NA	6.0e-2	NA	NA	NA
110	(*)	(**)				(.)			

1269

1270 **Supplementary Table 4.** Representative proteins of interest, reference organism and IDs.

Protein of interest	Reference organism	Protein ID
ZCRP-A	Thalassiosira pseudonana CCMP1335	3054 (JGI Thaps3*)
ZCRP-B	Thalassiosira pseudonana CCMP1335	938 (JGI Thaps3_bd**)
RUBISCO	Phaeodactylum tricornutum CCMP632	AAF07200.1 (NCBI)
ISIP1A	Thalassiosira oceanica CCMP1005	K0RCT3 (Uniprot)
ISIP2A	Phaeodactylum tricornutum CCMP632	B7FYL2 (Uniprot)
ISIP3	Phaeodactylum tricornutum CCMP632	B7G4H8 (Uniprot)
ZIP <u>1</u>	Phaeodactylum tricornutum CCMP632	46780 (JGI Phatr2†)
CDCA	Thalassiosira pseudonana CCMP1335	25840 (JGI Thaps3*)

^{1271 *}Joint Genome Institute (JGI) Thaps3 database

^{1272 (}https://mycocosm.jgi.doe.gov/Thaps3/Thaps3.home.html)

^{1273 **}Joint Genome Institute Thaps3_bd database

 $^{1274 \}qquad (https://mycocosm.jgi.doe.gov/Thaps3_bd/Thaps3_bd.home.html$

1275	[†] Joint Genome Institute CCAP 1055/1 v2.0 Phatr2, all models database
1276	(https://mycocosm.jgi.doe.gov/Phatr2/Phatr2.home.html)
1277	
1278	
1279	<u>Supplementary Table 5.</u> Summary of metaproteomic contigs detected in both the incubation
1 1280	biomass and in the water column at station 27 identified as ZCRP-A or ZIP homologs. For each
1281	contig, the top reference BLAST hit (see Supplementary Table 4) is listed with alignment
1282	statistics (E-value, percent identity). An example ortholog identified by SHOOT and the
1283	ortholog's corresponding UniProt protein description is also presented.
1284	
1285	
1286	Supplementary Table 65. Particulate Zn:P ratios measured in T. pseudonana cultured at various
1 1287	concentrations of Zn (log [Zn']) (Sunda and Huntsman 2005) compared to particulate Zn:P ratios
1288	measured at Station 27 of research cruise NBP18-01. Zn:C measurements by Sunda and
1289	Huntsman 2005 were converted to Zn:P using the Redfield ratio. Data is plotted in
1290	Supplementary Figure 6. Zn' refers to the sum of inorganic Zn metal complexes.
1291	⁺ Particulate P data measured directly in this study
1292	*Particulate P from Sunda 2005 data was estimated by converting particulate C measurements to
1293	P using the Redfield ratio (106C:1P).
1294	

Particulate Zn:P ratios at Station 27

	Particulat		Zn:P	
		Particulat		
Depth (m)	e Zn		(mol:mol	
		e P (mol) ⁺		
	(mol))	
100	1F 11	OF 00	15.04	
100	1E-11	8E-08	1E-04	
50	1E-11	1E-07	1E-04	
30	1E-11	1E-0/	1E-04	
25	3E-11	2E-07	2E-04	
23	3L-11	2L-07	211-04	
10	4E-11	2E-07	2E-04	
10	12 11			

Cellular Zn:P ratios of cultured *T. pseudonana* from Sunda and Huntsman 2005, Table

1.

			Particulat		Particulat	Zn:P	Growth
Experimen	Log	рН	e Zn	Particulat	e P	(mol:mol	rate (d-
t	[Zn']	P		e C (mol)			,
			(mol)		(mol)*)	1)
1	-12.05	8.2	3.3E-05	22	0.21	2E-04	0.1
1	-11.47	8.2	5.2E-05	15	0.14	4E-04	1.23
1	-10.87	8.2	1.2E-04	15	0.14	9E-04	1.62
1	-10.36	8.2	1.5E-04	15	0.14	1E-03	1.76
1	-9.82	8.2	1.8E-04	15	0.14	1E-03	1.76
1	-11.96	9	3.8E-05	15	0.14	3E-04	0.51
1	-11.38	9	8.5E-05	15	0.14	6E-04	1.12
1	-10.78	9	2.0E-04	15	0.14	1E-03	1.28
1	-10.27	9	4.1E-04	15	0.14	3E-03	1.42
1	-9.73	9	5.0E-04	15	0.14	4E-03	1.49
2	-11.82	8.2	4.9E-05	15	0.14	3E-04	0.64

2	-11.82	8.2	4.0E-05	15	0.14	3E-04	0.79
2	-10.87	8.2	1.3E-04	15	0.14	9E-04	1.45
2	-9.82	8.2	2.0E-04	15	0.14	1E-03	1.51
2	-11.71	9	5.8E-05	15	0.14	4E-04	0.73
2	-11.71	9	5.8E-05	15	0.14	4E-04	0.78
2	-10.76	9	1.9E-04	15	0.14	1E-03	1.39
2	-10.76	9	2.1E-04	15	0.14	1E-03	1.38
2	-9.71	9	4.3E-04	15	0.14	3E-03	1.44
2	-9.71	9	5.0E-04	15	0.14	4E-03	1.42
4	-11.82	8.2	2.8E-05	18.1	0.21	3E-04	0.72
4	-11.32	8.2	5.5E-05	15.2	0.13	4E-04	1.45
4	-10.82	8.2	1.3E-04	14.7	0.14	9E-04	2
4	-10.32	8.2	2.2E-04	15.1	0.14	2E-03	2.03
4	-9.82	8.2	2.6E-04	15.6	0.14	2E-03	2.04

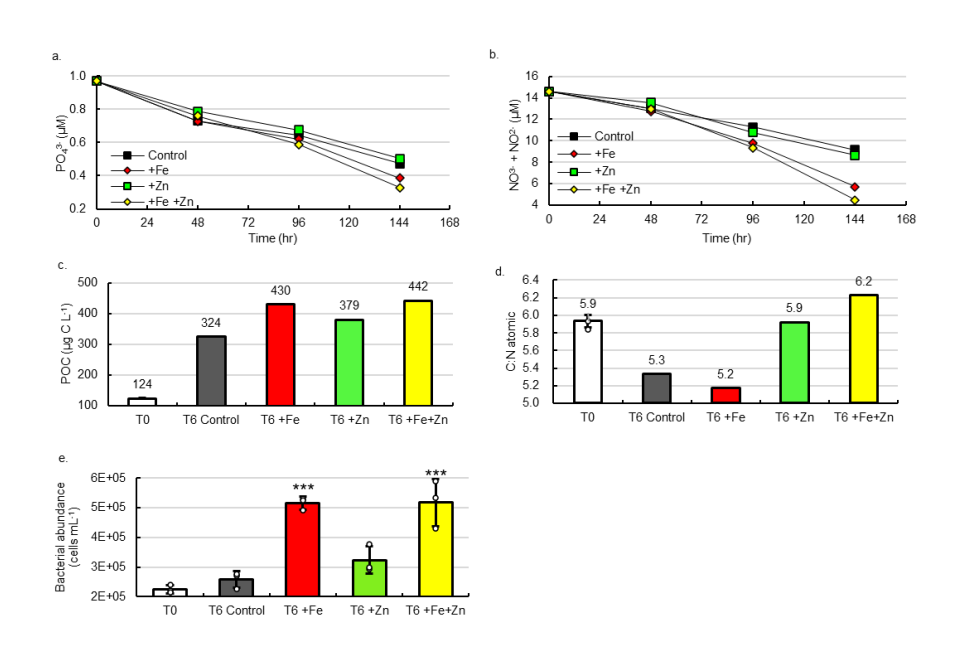
Supplementary Table 76. Reference seawater comparisons using the 2009 GEOTRACES

coastal surface seawater (GSC) standard.

This study GEOTRACES GSC consensus (nM)

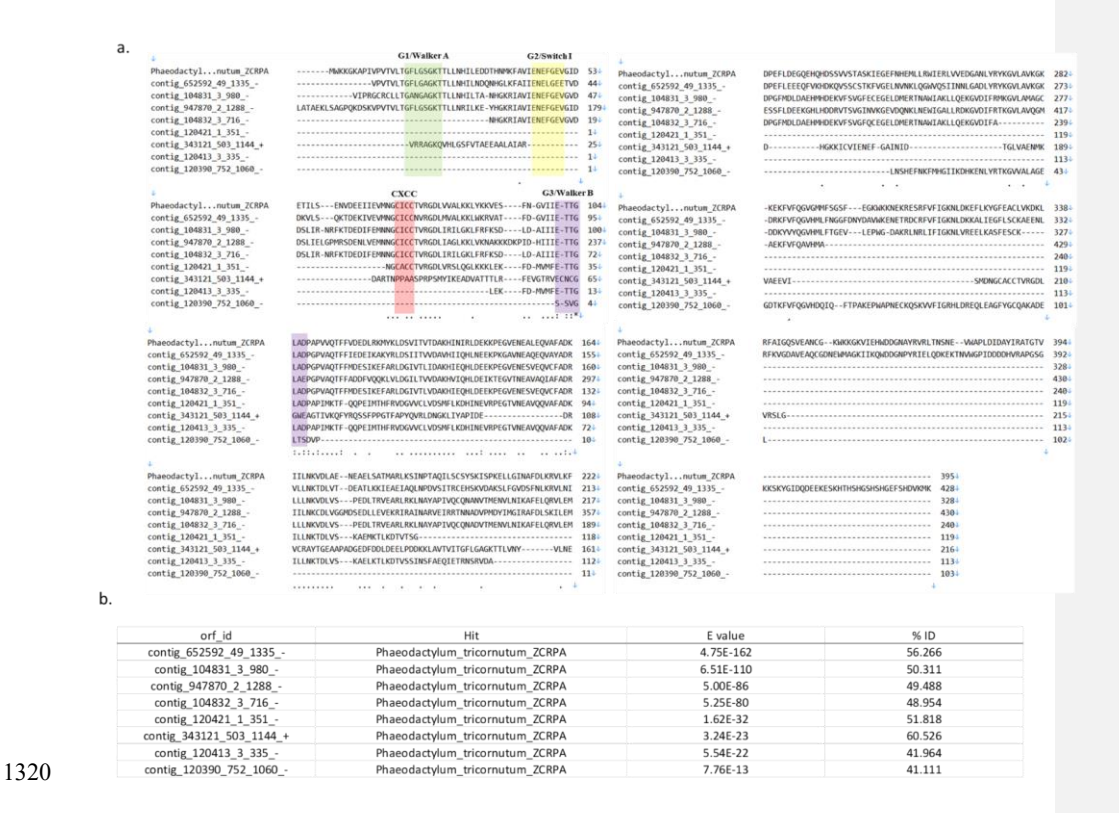
Metal	(n = 8)	
	(nM)	
Fe	1.6 ± 0.23	1.6 ± 0.12
Zn	1.4 ± 0.23	1.5 ± 0.10
Cd	0.4 ± 0.01	0.4 ± 0.02
Cu	1.3 ± 0.05	1.1 ± 0.15
Ni	4.2 ± 0.07	4.5 ± 0.21
Mn	2.1 ± 0.37	2.2 ± 0.08

Supplementary Figures



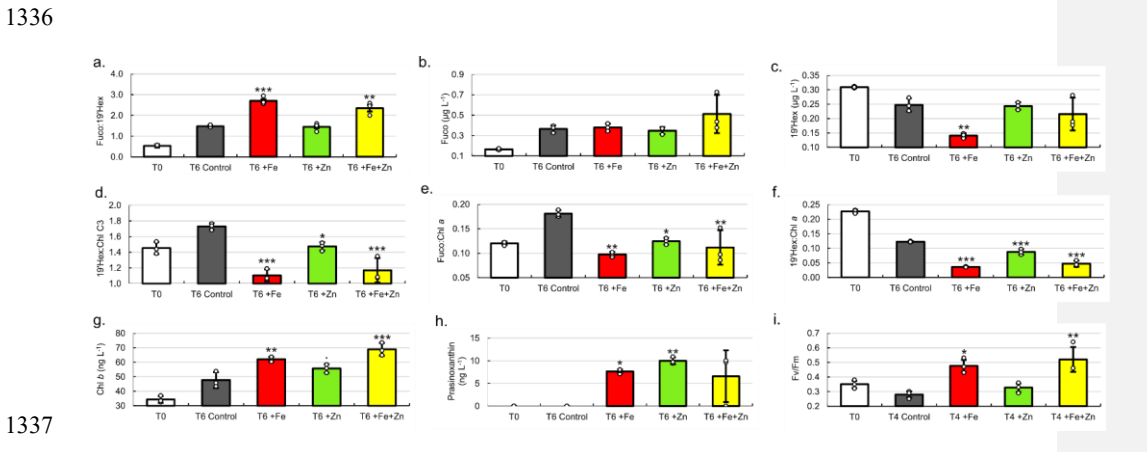
Supplementary Figure 1. Additional parameters measured in shipboard bottle incubations.

Time course decreases in (a) phosphate and (b) nitrite + nitrate. (c) total POC of biomass in each treatment at T6. (d) the atomic carbon:nitrogen (C:N) ratio of biomass in each treatment at T6, and (e) bacterial abundance. Significant differences among groups were found using one-way ANOVA and post-hoc Dunnett test (*** p < 0.001, ** p < 0.01, * p < 0.05). Error bars are the standard deviation of biological triplicates (n=3) with individual data points overlaid (white circles). Macronutrients, POC, and PON were measured in singlicate (n=1) from pooled biological triplicates.

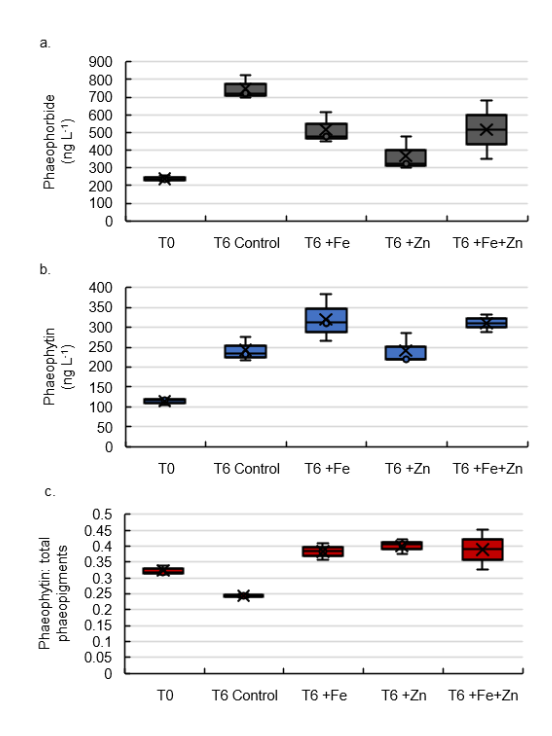


Supplementary Figure 2. Sequence alignments of ZCRP-A peptides detected in T6

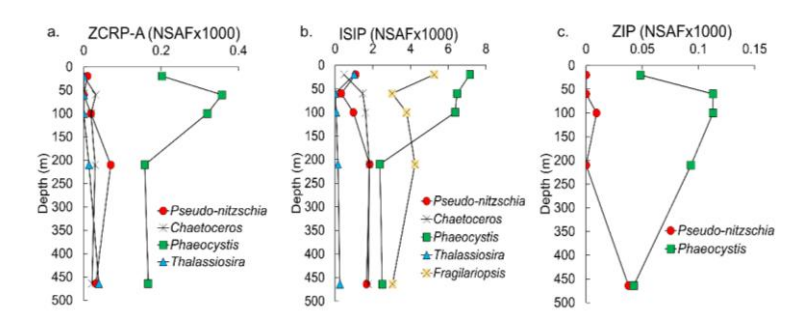
incubation biomass. (a) Sequence alignment of the *Phaeodactylum tricornutum* ZCRP-A protein compared to all ZCRP-A proteins detected in T6 incubation biomass. Alignment was generated using the MUSCLE algorithm with default parameters within MEGA11. Four conserved GTPase (G1/Walker A, G2/SwitchI, CXCC metal binding, and G3/Walker B) are labeled. (b) E values and percent% identities of the identified proteins with significant sequence similarity to *P. tricornutum* ZCRP-A aligned above.



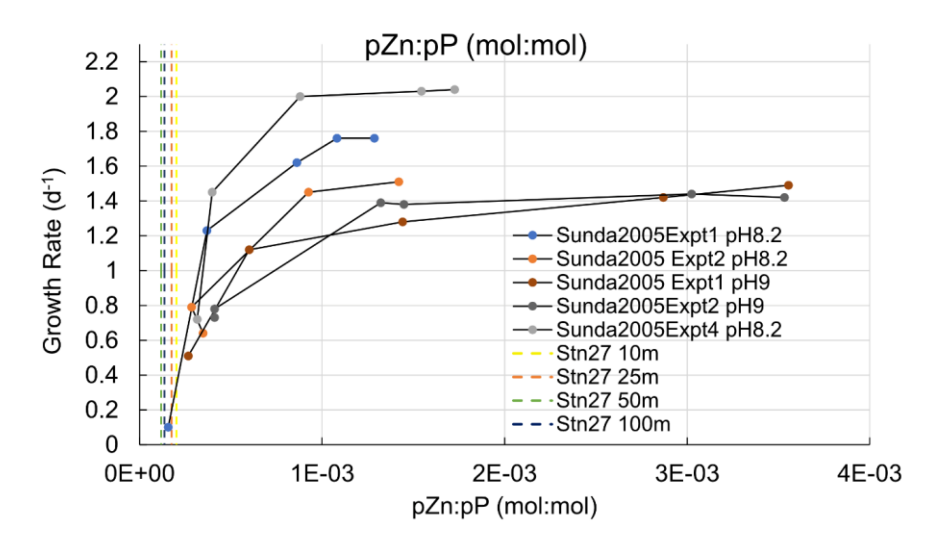
Supplementary Figure 3. Pigment analysis of T6 incubations. (a) ratio of fucoxanthin: 19'-Hex, (b) fucoxanthin, (c) 19-hexanoyloxyfucoxanthin (19'-Hex), (d) ratio of 19'-Hex: chlorophyll a, (e) ratio of fucoxanthin: chlorophyll a, (f) ratio of 19'-Hex: chlorophyll a, (g) chlorophyll b, (h) prasinoxanthin, and (i) maximum quantum efficiency (Fv/Fm) among treatments at T4. Significant differences among groups were found using one-way ANOVA and post-hoc Dunnett test (*** p < 0.001, ** p < 0.01, * p < 0.05, . p < 0.1). Data with error bars are presented as mean values \pm the standard deviation of biological triplicates (n=3) with individual data points overlaid (white circles).



Supplementary Figure 4. Phaeopigments measured in T6 incubation biomass. Abundances of (a) phaeophorbide and (b) phaeophytin, and (c) the ratio of phaeophytin: total phaeopigments (the sum of phaeophorbide and phaeophytin). Error bars are the standard deviation of biological triplicates (n=3).



Supplementary Figure 5. Depth profiles for proteins of interest at station 27 categorized by genus. Depth profiles of NSAF-normalized protein spectral counts of (a) ZCRP-A, (b), iron starvation induced proteins (ISIPs), and (c) ZIPs summed by genus. Proteins assigned to an individual genus were summed across all size fractions (0.2, 3 and 51 μm). ISIPs are the combined spectral counts of ISIP1A, ISIP2A and ISIP3.



Supplementary Figure 6. Comparison of particulate Zn: particulate P ratios measured in the water column at the experimental site to those ratios measured in culture studies of a Zn-limited diatom. Ratio of particulate Zn (pZn) and particulate phosphorus (pP) (pZn:pP) measured in the upper water column at the study site (station 27; vertical dashed lines) compared to pZn:pP measurements in Zn limitation studies of the diatom *Thalassiosira pseudonana* in culture by Sunda and Huntsman 2005.

1414	Allen, A. E. and others. 2008. Whole-cell response of the pennate diatom Phaeodactylum
1415	tricornutum to iron starvation. Proc. Natl. Acad. Sci. 105: 10438-10443.
1416	doi:10.1073/pnas.0711370105
1417	Altschul, S. F., W. Gish, W. Miller, E. W. Myers, and D. J. Lipman. 1990. Basic local alignment
1418	search tool. J. Mol. Biol. doi:10.1016/S0022-2836(05)80360-2
1419	Aramaki, T., R. Blanc-Mathieu, H. Endo, K. Ohkubo, M. Kanehisa, S. Goto, and H. Ogata.
1420	2020. KofamKOALA: KEGG Ortholog assignment based on profile HMM and adaptive
1421	score threshold A. Valencia [ed.]. Bioinformatics 36: 2251–2252.
1422	doi:10.1093/bioinformatics/btz859
1423	Arrigo, K. R., K. E. Lowry, and G. L. van Dijken. 2012. Annual changes in sea ice and
1424	phytoplankton in polynyas of the Amundsen Sea, Antarctica. Deep Sea Res. Part II Top.
1425	Stud. Oceanogr. 71-76: 5-15. doi:10.1016/j.dsr2.2012.03.006
1426	Baars, O., and P. L. Croot. 2011. The speciation of dissolved zinc in the Atlantic sector of the
1427	Southern Ocean. Deep Sea Res. Part II Top. Stud. Oceanogr. 58: 2720–2732.
1428	doi:10.1016/j.dsr2.2011.02.003
1429	Balestra, C., L. Alonso-Sáez, J. M. Gasol, and R. Casotti. 2011. Group-specific effects on coasta
1430	bacterioplankton of polyunsaturated aldehydes produced by diatoms. Aquat. Microb.
1431	Ecol. doi:10.3354/ame01486
1432	Behnke, J., and J. LaRoche. 2020. Iron uptake proteins in algae and the role of Iron Starvation-
1433	Induced Proteins (ISIPs). Eur. J. Phycol. 55: 339–360.
1434	doi:10.1080/09670262.2020.1744039

1435	Bender, S. J. and others. 2018. Colony formation in Phaeocystis antarctica: connecting molecular
1436	mechanisms with iron biogeochemistry. Biogeosciences 15: 4923-4942. doi:10.5194/bg-
1437	15-4923-2018
1438	Blaby-Haas, C. E., and S. S. Merchant. 2012. The ins and outs of algal metal transport. Biochim.
1439	Biophys. Acta - Mol. Cell Res. 1823: 1531–1552. doi:10.1016/j.bbamcr.2012.04.010
1440	Bolger, A. M., M. Lohse, and B. Usadel. 2014. Trimmomatic: a flexible trimmer for Illumina
1441	sequence data. Bioinformatics 30: 2114–2120. doi:10.1093/bioinformatics/btu170
1442	Browning, T. J., and C. M. Moore. 2023. Global analysis of ocean phytoplankton nutrient
1443	limitation reveals high prevalence of co-limitation. Nat. Commun. 14: 5014.
1444	doi:10.1038/s41467-023-40774-0
1445	Bruland, K. W. 1980. Oceanographic distributions of cadmium, zinc, nickel, and copper in the
1446	North Pacific. Earth Planet. Sci. Lett. 47: 176–198. doi:10.1016/0012-821X(80)90035-7
1447	Bruland, K. W. 1989. Complexation of zinc by natural organic ligands in the central North
1448	Pacific. Limnol. Oceanogr. 34: 269–285. doi:10.4319/lo.1989.34.2.0269
1449	Buitenhuis, E. T., K. R. Timmermans, and H. J. W. de Baar. 2003. Zinc-bicarbonate colimitation
1450	of Emiliania huxleyi. Limnol. Oceanogr. 48: 1575–1582. doi:10.4319/lo.2003.48.4.1575
1451	Chavez, F. P., J. Sevadjian, C. Wahl, J. Friederich, and G. E. Friederich. 2018. Measurements of
1452	pCO2 and pH from an autonomous surface vehicle in a coastal upwelling system. Deep
1453	Sea Res. Part II Top. Stud. Oceanogr. 151: 137–146. doi:10.1016/j.dsr2.2017.01.001
1454	Coale, K. H., R. Michael Gordon, and X. Wang. 2005. The distribution and behavior of
1455	dissolved and particulate iron and zinc in the Ross Sea and Antarctic circumpolar current
1456	along 170°W. Deep Sea Res. Part Oceanogr. Res. Pap. 52: 295–318.
1457	doi:10.1016/j.dsr.2004.09.008

1458	Coale, K. H., X. Wang, S. J. Tanner, and K. S. Johnson. 2003. Phytoplankton growth and
1459	biological response to iron and zinc addition in the Ross Sea and Antarctic Circumpolar
1460	Current along 170°W. Deep Sea Res. Part II Top. Stud. Oceanogr. 50: 635-653.
1461	doi:10.1016/S0967-0645(02)00588-X
1462	Cochlan, W. P., D. A. Bronk, and K. H. Coale. 2002. Trace metals and nitrogenous nutrition of
1463	Antarctic phytoplankton: experimental observations in the Ross Sea. Deep Sea Res. Part
1464	II Top. Stud. Oceanogr. 49: 3365–3390. doi:10.1016/S0967-0645(02)00088-7
1465	Cox, A. D., A. E. Noble, and M. A. Saito. 2014. Cadmium enriched stable isotope uptake and
1466	addition experiments with natural phytoplankton assemblages in the Costa Rica
1467	Upwelling Dome. Mar. Chem. 166: 70-81. doi:10.1016/j.marchem.2014.09.009
1468	Crameri, F. 2023. Scientific colour maps.doi:10.5281/ZENODO.1243862
1469	Crawford, D. W. and others. 2003a. Influence of zinc and iron enrichments on phytoplankton
1470	growth in the northeastern subarctic Pacific Limitation of biomass and primary
1471	production of phyto-plankton by dissolved iron (Fe) in high-nutrient, low-chlo.
1472	Crawford, D. W. and others. 2003b. Influence of zinc and iron enrichments on phytoplankton
1473	growth in the northeastern subarctic Pacific. Limnol. Oceanogr. 48: 1583-1600.
1474	doi:10.4319/lo.2003.48.4.1583
1475	Cullen, J. T., T. W. Lane, F. M. M. Morel, and R. M. Sheerell. 1999. Modulation of cadmium
1476	uptake in phytoplankton by seawater CO2 concentration. Nature. doi:10.1038/46007
1477	Cullen, J. T., and R. M. Sherrell. 2005. Effects of dissolved carbon dioxide, zinc, and manganese
1478	on the cadmium to phosphorus ratio in natural phytoplankton assemblages. Limnol.
1479	Oceanogr. 50 : 1193–1204. doi:10.4319/lo.2005.50.4.1193

1480	Cutter, G. A., and K. W. Bruland. 2012. Rapid and noncontaminating sampling system for trace
1481	elements in global ocean surveys. Limnol. Oceanogr. Methods.
1482	doi:10.4319/lom.2012.10.425
1483	Dai, M. and others. 2022. Carbon Fluxes in the Coastal Ocean: Synthesis, Boundary Processes,
1484	and Future Trends. Annu. Rev. Earth Planet. Sci. 50: 593-626. doi:10.1146/annurev-
1485	earth-032320-090746
1486	DeJong, H. B., R. B. Dunbar, D. Mucciarone, and D. A. Koweek. 2015. Carbonate saturation
1487	state of surface waters in the Ross Sea and Southern Ocean: controls and implications for
1488	the onset of aragonite undersaturation. Biogeosciences 12: 6881-6896. doi:10.5194/bg-
1489	12-6881-2015
1490	Dickson, A. G., C. L. Sabine, and J. R. Christian, 2007. Guide to best practices for ocean CO2
1491	measurement. North Pacific Marine Science Organization.
1492	DiTullio, G. R. and others. 2000. Rapid and early export of Phaeocystis antarctica blooms in the
1493	Ross Sea, Antarctica. Nature. doi:10.1038/35007061
1494	DiTullio, G. R., N. Garcia, S. F. Riseman, and P. N. Sedwick. 2007. Effects of iron concentration
1495	on pigment composition in Phaeocystis antarctica grown at low irradiance.
1496	Biogeochemistry 83: 71-81. doi:10.1007/s10533-007-9080-8
1497	DiTullio, G. R., M. E. Geesey, A. Leventer, and M. P. Lizotte. 2003. Algal pigment ratios in the
1498	Ross Sea: Implications for Chemtax analysis of Southern Ocean data, p. 35-51. In.
1499	DiTullio, G. R., and W. O. Smith. 1996. Spatial patterns in phytoplankton biomass and pigment
1500	distributions in the Ross Sea. J. Geophys. Res. Oceans 101: 18467–18477.
1501	doi:10.1029/96JC00034

1502	Dreux Chappell, P., J. Vedmati, K. E. Selph, H. A. Cyr, B. D. Jenkins, M. R. Landry, and J. W.
1503	Moffett. 2016. Preferential depletion of zinc within Costa Rica upwelling dome creates
1504	conditions for zinc co-limitation of primary production. J. Plankton Res. 38: 244–255.
1505	doi:10.1093/plankt/fbw018
1506	Eddy, S. R. 2011. Accelerated Profile HMM Searches W.R. Pearson [ed.]. PLoS Comput. Biol.
1507	7: e1002195. doi:10.1371/journal.pcbi.1002195
1508	Edmonds, K. A., M. R. Jordan, and D. P. Giedroc. 2021. COG0523 proteins: a functionally
1509	diverse family of transition metal-regulated G3E P-loop GTP hydrolases from bacteria to
1510	man. Metallomics 13. doi:10.1093/mtomcs/mfab046
1511	Ellwood, M. J. 2004. Zinc and cadmium speciation in subantarctic waters east of New Zealand.
1512	Mar. Chem. doi:10.1016/j.marchem.2004.01.005
1513	Emms, D. M., and S. Kelly. 2022. SHOOT: phylogenetic gene search and ortholog inference.
1514	Genome Biol. 23. doi:10.1186/s13059-022-02652-8
1515	Etheridge, D. M., L. P. Steele, R. L. Langenfelds, R. J. Francey, JM. Barnola, and V. I.
1516	Morgan. 1996. Natural and anthropogenic changes in atmospheric CO 2 over the last
1517	1000 years from air in Antarctic ice and firn. J. Geophys. Res. Atmospheres 101: 4115-
1518	4128. doi:10.1029/95JD03410
1519	Fitzwater, S. E., K. S. Johnson, R. M. Gordon, K. H. Coale, and W. O. Smith. 2000. Trace metal
1520	concentrations in the Ross Sea and their relationship with nutrients and phytoplankton
1521	growth. Deep-Sea Res. Part II Top. Stud. Oceanogr. 47: 3159-3179. doi:10.1016/S0967-
1522	0645(00)00063-1

1523	Fourquez, M., M. Bressac, S. L. Deppeler, M. Ellwood, I. Obernosterer, T. W. Trull, and P. W.
1524	Boyd. 2020. Microbial Competition in the Subpolar Southern Ocean: An Fe-C Co-
1525	limitation Experiment. Front. Mar. Sci. 6: 776. doi:10.3389/fmars.2019.00776
1526	Franck, V., K. Bruland, D. Hutchins, and M. Brzezinski. 2003. Iron and zinc effects on silicic
1527	acid and nitrate uptake kinetics in three high-nutrient, low-chlorophyll (HNLC) regions.
1528	Mar. Ecol. Prog. Ser. 252: 15–33. doi:10.3354/meps252015
1529	Fukuda, R., Y. Sohrin, N. Saotome, H. Fukuda, T. Nagata, and I. Koike. 2000. East—west
1530	gradient in ectoenzyme activities in the subarctic Pacific: Possible regulation by zinc.
1531	Limnol. Oceanogr. 45: 930-939. doi:10.4319/lo.2000.45.4.0930
1532	Harrison, C. S., M. C. Long, N. S. Lovenduski, and J. K. Moore. 2018. Mesoscale Effects on
1533	Carbon Export: A Global Perspective. Glob. Biogeochem. Cycles 32: 680-703.
1534	doi:10.1002/2017GB005751
1535	Jakuba, R. W., M. A. Saito, J. W. Moffett, and Y. Xu. 2012. Dissolved zinc in the subarctic
1536	North Pacific and Bering Sea: Its distribution, speciation, and importance to primary
1537	producers. Glob. Biogeochem. Cycles. doi:10.1029/2010GB004004
1538	Jensen, E. L., S. C. Maberly, and B. Gontero. 2020a. Insights on the Functions and
1539	Ecophysiological Relevance of the Diverse Carbonic Anhydrases in Microalgae. Int. J.
1540	Mol. Sci. 21: 2922. doi:10.3390/ijms21082922
1541	Jensen, L. T., N. J. Wyatt, W. M. Landing, and J. N. Fitzsimmons. 2020b. Assessment of the
1542	stability, sorption, and exchangeability of marine dissolved and colloidal metals. Mar.
1543	Chem. 220: 103754. doi:10.1016/j.marchem.2020.103754
1544	Jiang, L. and others. 2023. Global Surface Ocean Acidification Indicators From 1750 to 2100. J.
1545	Adv. Model. Earth Syst. 15: e2022MS003563. doi:10.1029/2022MS003563

1546	Keeling, C. D., R. B. Bacastow, A. E. Bainbridge, C. A. Ekdahl, P. R. Guenther, L. S.
1547	Waterman, and J. F. S. Chin. 1976. Atmospheric carbon dioxide variations at Mauna Loa
1548	Observatory, Hawaii. Tellus Dyn. Meteorol. Oceanogr. 28: 538.
1549	doi:10.3402/tellusa.v28i6.11322
1550	Kell, R. M. and others. 2024. High metabolic zinc demand within native Amundsen and Ross sea
1551	phytoplankton communities determined by stable isotope uptake rate measurements.
1552	Biogeosciences 21: 5685-5706. doi:10.5194/bg-21-5685-2024
1553	Kellogg, R. M. and others. 2022a. Adaptive responses of marine diatoms to zinc scarcity and
1554	ecological implications. Nat. Commun. 2022 131 13: 1-13. doi:10.1038/s41467-022-
1555	29603-у
1556	Kellogg, R. M., M. R. McIlvin, J. Vedamati, B. S. Twining, J. W. Moffett, A. Marchetti, D. M.
1557	Moran, and M. A. Saito. 2020. Efficient zinc/cobalt inter-replacement in northeast Pacific
1558	diatoms and relationship to high surface dissolved Co: Zn ratios. Limnol. Oceanogr. 65:
1559	2557–2582. doi:10.1002/lno.11471
1560	Kellogg, R. M., D. M. Moran, M. R. McIlvin, A. V. Subhas, A. E. Allen, and M. A. Saito.
1561	2022b. Lack of a Zn/Co substitution ability in the polar diatom Chaetoceros neogracile
1562	RS19. Limnol. Oceanogr. 67: 2265–2280. doi:10.1002/lno.12201
1563	Krogh, A., B. Larsson, G. von Heijne, and E. L. L. Sonnhammer. 2001. Predicting
1564	transmembrane protein topology with a hidden markov model: application to complete
1565	genomes11Edited by F. Cohen. J. Mol. Biol. 305 : 567–580. doi:10.1006/jmbi.2000.4315
1566	Krumhardt, K. M., N. S. Lovenduski, M. D. Iglesias-Rodriguez, and J. A. Kleypas. 2017.
1567	Coccolithophore growth and calcification in a changing ocean. Prog. Oceanogr. 159:
1568	276–295. doi:10.1016/j.pocean.2017.10.007

1569	Lampe, R. H. and others. 2018. Different iron storage strategies among bloom-forming diatoms.
1570	Proc. Natl. Acad. Sci. 115. doi:10.1073/pnas.1805243115
1571	Lane, T. W., and F. M. Morel. 2000a. A biological function for cadmium in marine diatoms.
1572	Proc. Natl. Acad. Sci. U. S. A. 97: 4627–31. doi:10.1073/pnas.090091397
1573	Lane, T. W., and F. M. M. Morel. 2000b. Regulation of Carbonic Anhydrase Expression by
1574	Zinc, Cobalt, and Carbon Dioxide in the Marine Diatom Thalassiosira weissflogii. Plant
1575	Physiol. 123: 345–352. doi:10.1104/pp.123.1.345
1576	Lauvset, S. K. and others. 2022. GLODAPv2.2022: the latest version of the global interior ocean
1577	biogeochemical data product. Earth Syst. Sci. Data 14: 5543-5572. doi:10.5194/essd-14-
1578	5543-2022
1579	Lhospice, S. and others. 2017. Pseudomonas aeruginosa zinc uptake in chelating environment is
1580	primarily mediated by the metallophore pseudopaline. Sci. Rep. 7: 17132.
1581	doi:10.1038/s41598-017-16765-9
1582	Li, B., and C. N. Dewey. 2011. RSEM: accurate transcript quantification from RNA-Seq data
1583	with or without a reference genome. BMC Bioinformatics 12: 323. doi:10.1186/1471-
1584	2105-12-323
1585	Lohan, M. C., P. J. Statham, and D. W. Crawford. 2002. Total dissolved zinc in the upper water
1586	column of the subarctic North East Pacific. Deep Sea Res. Part II Top. Stud. Oceanogr.
1587	49 : 5793–5808. doi:10.1016/S0967-0645(02)00215-1
1588	Lu, X., and H. Zhu. 2005. Tube-Gel Digestion. Mol. Cell. Proteomics 4: 1948–1958.
1589	doi:10.1074/mcp.m500138-mcp200
1590	Mangoni, O., M. Saggiomo, F. Bolinesi, M. Castellano, P. Povero, V. Saggiomo, and G. R.
1591	DiTullio. 2019. Phaeocystis antarctica unusual summer bloom in stratified antarctic

1592	coastal waters (Terra Nova Bay, Ross Sea). Mar. Environ. Res.
1593	doi:10.1016/j.marenvres.2019.05.012
1594	Martin, J. H., S. E. Fitzwater, and R. M. Gordon. 1990. Iron deficiency limits phytoplankton
1595	growth in Antarctic waters. Glob. Biogeochem. Cycles 4: 5-12.
1596	doi:10.1029/GB004i001p00005
1597	Mazzotta, M. G., M. R. McIlvin, D. M. Moran, D. T. Wang, K. D. Bidle, C. H. Lamborg, and M.
1598	A. Saito. 2021. Characterization of the metalloproteome of Pseudoalteromonas (BB2-
1599	AT2): biogeochemical underpinnings for zinc, manganese, cobalt, and nickel cycling in a
1600	ubiquitous marine heterotroph. Metallomics 13. doi:10.1093/mtomcs/mfab060
1601	McIlvin, M. R., and M. A. Saito. 2021. Online Nanoflow Two-Dimension Comprehensive
1602	Active Modulation Reversed Phase-Reversed Phase Liquid Chromatography High-
1603	Resolution Mass Spectrometry for Metaproteomics of Environmental and Microbiome
1604	Samples. J. Proteome Res. 20: 4589–4597. doi:10.1021/acs.jproteome.1c00588
1605	Middag, R., H. J. W. De Baar, and K. W. Bruland. 2019. The Relationships Between Dissolved
1606	Zinc and Major Nutrients Phosphate and Silicate Along the GEOTRACES GA02
1607	Transect in the West Atlantic Ocean. Glob. Biogeochem. Cycles 33: 63-84.
1608	doi:10.1029/2018GB006034
1609	Milner, M. J., J. Seamon, E. Craft, and L. V. Kochian. 2013. Transport properties of members of
1610	the ZIP family in plants and their role in Zn and Mn homeostasis. J. Exp. Bot. 64: 369-
1611	381. doi:10.1093/jxb/ers315
1612	Moore, C. M. and others. 2013. Processes and patterns of oceanic nutrient limitation. Nat.
1613	Geosci, 6: 701–710, doi:10.1038/ngeo1765

1614	Morel, F. M. M., J. R. Reinfelder, S. B. Roberts, C. P. Chamberlain, J. G. Lee, and D. Yee. 1994.
1615	Zinc and carbon co-limitation of marine phytoplankton. Nature 369: 740-742.
1616	doi:10.1038/369740A0
1617	Mortazavi, A., B. A. Williams, K. McCue, L. Schaeffer, and B. Wold. 2008. Mapping and
1618	quantifying mammalian transcriptomes by RNA-Seq. Nat. Methods 5: 621-628.
1619	doi:10.1038/nmeth.1226
1620	Obernosterer, I., M. Fourquez, and S. Blain. 2015. Fe and C co-limitation of heterotrophic
1621	bacteria in the naturally fertilized region off the Kerguelen Islands. Biogeosciences 12:
1622	1983–1992. doi:10.5194/bg-12-1983-2015
1623	Podell, S., and T. Gaasterland. 2007. DarkHorse: a method for genome-wide prediction of
1624	horizontal gene transfer. Genome Biol. 8: R16. doi:10.1186/gb-2007-8-2-r16
1625	Rapp, I., C. Schlosser, D. Rusiecka, M. Gledhill, and E. P. Achterberg. 2017. Automated
1626	preconcentration of Fe, Zn, Cu, Ni, Cd, Pb, Co, and Mn in seawater with analysis using
1627	high-resolution sector field inductively-coupled plasma mass spectrometry. Anal. Chim.
1628	Acta. doi:10.1016/j.aca.2017.05.008
1629	Redfield, A. C. 1958. The Biological Control of Chemical Factors in the Environment. Am. Sci.
1630	doi:10.2307/27828530
1631	Rho, M., H. Tang, and Y. Ye. 2010. FragGeneScan: predicting genes in short and error-prone
1632	reads. Nucleic Acids Res. 38: e191-e191. doi:10.1093/nar/gkq747
1633	Riebesell, U., D. A. Wolf-Gladrow, and V. Smetacek. 1993. Carbon dioxide limitation of marine
1634	phytoplankton growth rates. Nature 361: 249–251. doi:10.1038/361249a0

1635	Robbins, L. L. and others. 2018. Spatial and Temporal Variability of pCO_2 , Carbon Fluxes, and
1636	Saturation State on the West Florida Shelf. J. Geophys. Res. Oceans 123: 6174-6188.
1637	doi:10.1029/2018JC014195
1638	Roshan, S., T. DeVries, J. Wu, and G. Chen. 2018. The Internal Cycling of Zinc in the Ocean.
1639	Glob. Biogeochem. Cycles 32: 1833–1849. doi:10.1029/2018GB006045
1640	Saito, M. A., and T. J. Goepfert. 2008. Zinc-cobalt colimitation of <i>Phaeocystis antarctica</i> .
1641	Limnol. Oceanogr. 53: 266-275. doi:10.4319/lo.2008.53.1.0266
1642	Saito, M. A., T. J. Goepfert, and J. T. Ritt. 2008. Some thoughts on the concept of colimitation:
1643	Three definitions and the importance of bioavailability. Limnol. Oceanogr. 53: 276–290.
1644	doi:10.4319/lo.2008.53.1.0276
1645	Schanke, N. L., F. Bolinesi, O. Mangoni, C. Katlein, P. Anhaus, M. Hoppmann, P. A. Lee, and
1646	G. R. DiTullio. 2021. Biogeochemical and ecological variability during the late summer-
1647	early autumn transition at an ice-floe drift station in the Central Arctic Ocean. Limnol.
1648	Oceanogr. doi:10.1002/lno.11676
1649	Scharek, R., M. A. Van Leeuwe, and H. J. W. De Baar. 1997. Responses of Southern Ocean
1650	phytoplankton to the addition of trace metals. Deep-Sea Res. Part II Top. Stud. Oceanogram
1651	doi:10.1016/S0967-0645(96)00074-4
1652	Schmieder, R., Y. W. Lim, and R. Edwards. 2012. Identification and removal of ribosomal RNA
1653	sequences from metatranscriptomes. Bioinformatics 28: 433–435.
1654	doi:10.1093/bioinformatics/btr669
1655	Schneider, B., and J. D. Müller. 2018. Biogeochemical transformations in the Baltic Sea:
1656	observations through carbon dioxide glasses, Springer.

1657	Sharma, D., H. Biswas, S. Silori, D. Bandyopadhyay, A. urRahman Shaik, D. Cardinal, M.
1658	Mandeng-Yogo, and D. Ray. 2020. Impacts of Zn and Cu enrichment under ocean
1659	acidification scenario on a phytoplankton community from tropical upwelling system.
1660	Mar. Environ. Res. 155: 104880. doi:10.1016/j.marenvres.2020.104880
1661	Sharp, J. D., D. Pierrot, M. P. Humphreys, JM. Epitalon, J. C. Orr, E. R. Lewis, and D. W. R.
1662	Wallace. 2023. CO2SYSv3 for MATLAB.doi:10.5281/ZENODO.3950562
1663	Shim, J., D. Kim, Y. C. Kang, J. H. Lee, ST. Jang, and CH. Kim. 2007. Seasonal variations in
1664	pCO2 and its controlling factors in surface seawater of the northern East China Sea. Cont.
1665	Shelf Res. 27: 2623–2636. doi:10.1016/j.csr.2007.07.005
1666	Sieber, M., T. M. Conway, G. F. de Souza, C. S. Hassler, M. J. Ellwood, and D. Vance. 2020.
1667	Cycling of zinc and its isotopes across multiple zones of the Southern Ocean: Insights
1668	from the Antarctic Circumnavigation Expedition. Geochim. Cosmochim. Acta.
1669	doi:10.1016/j.gca.2019.09.039
1670	Smith, W. O., A. R. Shields, J. A. Peloquin, G. Catalano, S. Tozzi, M. S. Dinniman, and V. A.
1671	Asper. 2006. Interannual variations in nutrients, net community production, and
1672	biogeochemical cycles in the Ross Sea. Deep-Sea Res. Part II Top. Stud. Oceanogr.
1673	doi:10.1016/j.dsr2.2006.02.014
1674	Sperfeld, E., D. Raubenheimer, and A. Wacker. 2016. Bridging factorial and gradient concepts
1675	of resource co-limitation: towards a general framework applied to consumers J. Grover
1676	[ed.]. Ecol. Lett. 19: 201–215. doi:10.1111/ele.12554
1677	Subhas, A. V., J. F. Adkins, S. Dong, N. E. Rollins, and W. M. Berelson. 2019. The carbonic
1678	anhydrase activity of sinking and suspended particles in the North Pacific Ocean. Limnol.
1679	Oceanogr. 65: 637–651. doi:10.1002/lno.11332

1680	Sun, Y., P. Debeljak, and I. Obernosterer. 2021. Microbial iron and carbon metabolism as
1681	revealed by taxonomy-specific functional diversity in the Southern Ocean. ISME J. 15:
1682	2933–2946. doi:10.1038/s41396-021-00973-3
1683	Sunda, W. G., and S. A. Huntsman. 1995. Cobalt and zinc interreplacement in marine
1684	phytoplankton: Biological and geochemical implications. Limnol. Oceanogr. 40: 1404-
1685	1417. doi:10.4319/lo.1995.40.8.1404
1686	Sunda, W. G., and S. A. Huntsman. 2000. Effect of Zn, Mn, and Fe on Cd accumulation in
1687	phytoplankton: Implications for oceanic Cd cycling. Limnol. Oceanogr. 45: 1501–1516.
1688	doi:10.4319/lo.2000.45.7.1501
1689	Sunda, W. G., and S. A. Huntsman. 2005. Effect of CO 2 supply and demand on zinc uptake and
1690	growth limitation in a coastal diatom. Limnol. Oceanogr. 50: 1181-1192.
1691	doi:10.4319/lo.2005.50.4.1181
1692	Takahashi, T., S. C. Sutherland, and A. Kozyr. 2020. Global Ocean Surface Water Partial
1693	Pressure of CO2 Database (LDEO Database Version 2019): Measurements Performed
1694	During 1957-2019 (NCEI Accession 0160492). NOAA Natl. Cent. Environ. Inf.
1695	Tatusov, R. L. and others. 2003. The COG database: an updated version includes eukaryotes.
1696	BMC Bioinformatics 4: 41. doi:10.1186/1471-2105-4-41
1697	Tortell, P. D., M. C. Long, C. D. Payne, AC. Alderkamp, P. Dutrieux, and K. R. Arrigo. 2012.
1698	Spatial distribution of pCO2, Δ O2/Ar and dimethylsulfide (DMS) in polynya waters and
1699	the sea ice zone of the Amundsen Sea, Antarctica. Deep Sea Res. Part II Top. Stud.
1700	Oceanogr. 71–76: 77–93. doi:10.1016/j.dsr2.2012.03.010

1701	Tortell, P. D., C. Payne, C. Gueguen, R. F. Strzepek, P. W. Boyd, and B. Rost. 2008. Inorganic
1702	carbon uptake by Southern Ocean phytoplankton. Limnol. Oceanogr. 53: 1266–1278.
1703	doi:10.4319/lo.2008.53.4.1266
1704	Twining, B. S., and S. B. Baines. 2013. The trace metal composition of marine phytoplankton.
1705	Annu. Rev. Mar. Sci. 5: 191–215. doi:10.1146/annurev-marine-121211-172322
1706	Valerio, A. M., M. Kampel, N. D. Ward, H. O. Sawakuchi, A. C. Cunha, and J. E. Richey. 2021.
1707	CO2 partial pressure and fluxes in the Amazon River plume using in situ and remote
1708	sensing data. Cont. Shelf Res. 215: 104348. doi:10.1016/j.csr.2021.104348
1709	Wuttig, K. and others. 2019. Critical evaluation of a seaFAST system for the analysis of trace
1710	metals in marine samples. Talanta. doi:10.1016/j.talanta.2019.01.047
1711	Wyatt, N. J., A. Milne, E. M. S. Woodward, A. P. Rees, T. J. Browning, H. A. Bouman, P. J.
1712	Worsfold, and M. C. Lohan. 2014. Biogeochemical cycling of dissolved zinc along the
1713	GEOTRACES South Atlantic transect GA10 at 40°S. Glob. Biogeochem. Cycles 28: 44-
1714	56. doi:10.1002/2013GB004637
1715	Xu, Y., D. Shi, L. Aristilde, and F. M. M. Morel. 2012. The effect of pH on the uptake of zinc
1716	and cadmium in marine phytoplankton: Possible role of weak complexes. Limnol.
1717	Oceanogr. doi:10.4319/lo.2012.57.1.0293
1718	Ye, N. and others. 2022. The role of zinc in the adaptive evolution of polar phytoplankton. Nat.
1719	Ecol. Evol. 6 : 965–978. doi:10.1038/s41559-022-01750-x
1720	Zhang, Y., Z. Wen, M. P. Washburn, and L. Florens. 2010. Refinements to Label Free Proteome
1721	Quantitation: How to Deal with Peptides Shared by Multiple Proteins. Anal. Chem. 82:
1722	2272–2281. doi:10.1021/ac9023999